# In situ measurements of strongly interacting Lithium system

Daniele Baldolini

Thesis submitted to The University of Nottingham for the degree of MSc (By Research), September 2017



# Contents

**List of Figures** **3**

**Abstract** **6**

**Acknowledgements** **7**

**1 Introduction** **9**

**2 Theoretical background** **13**

2.1 Properties of Alkali atoms . . . . . 13

2.1.1 Atomic structure . . . . . 13

2.2 Interaction with static magnetic fields . . . . . 19

2.3 Light and Matter interaction . . . . . 22

2.4 Scattering Theory . . . . . 24

2.4.1 Feshbach resonance . . . . . 27

**3 Experimental Techniques** **29**

3.1 Laser Cooling . . . . . 29

3.1.1 Scattering Force . . . . . 29

3.1.2 Zeeman slower . . . . . 31

3.2 The Magneto Optical Trap . . . . . 33

3.2.1 The Doppler limit . . . . . 34

3.2.2 Prospects on Sub-Doppler Cooling . . . . . 35

3.3 Optical Dipole Trap . . . . . 36

3.3.1 The focused beam trap . . . 38
3.3.2 Evaporative Cooling . . . 39
3.4 Imaging . . . 42
3.4.1 Measuring the Temperature . . . 43

**4 Experimental apparatus** **47**

4.1 Laser Setup . . . 47
4.1.1 Overview . . . 48
4.2 The Magneto Optical Trap . . . 49
4.2.1 Compression phase and transfer into Dipole Trap . . . 51
4.2.2 Sub-Doppler cooling of Lithium . . . 53
4.3 Dipole Trap . . . 55
4.3.1 Trapping frequencies . . . 57
4.3.2 Power stabilisation . . . 59
4.4 Evaporative Cooling . . . 60

**5 $^6Li_2$ BEC and In situ characterization** **63**

5.1 $^6Li_2$ molecular BEC . . . 63
5.1.1 Ideal gas . . . 65
5.1.2 Semi-Ideal approximation . . . 68
5.1.3 Hartree-Fock method . . . 69
5.1.4 Experimental comparison . . . 70

**6 Conclusions** **73**

**Bibliography** **75**

# List of Figures

**Chapter 2**


2.1 Energy splittings of the ground end excited states, and the relative fine and hyperfine structure. . . . . 17

2.2 $D_1$ and $D_2$ Li lines with relative wavelenghts. Splittings not to scale . 18

2.3 Calculated Breit-Rabi diagram of the $^6$Li $^2P_{3/2}$ manifold . . . . . 21

2.4 Calculated Breit-Rabi diagram of the $^6$Li $^2S_{1/2}$ manifold . . . . . 22

2.5 Effective potential $V_{\text{eff}}$ for the radial part of the partial waves . . . . . 27

2.6 Scattering length as a function of magnetic field for $^6$Li atoms in the lowest ground state . . . . . 28


**Chapter 3**


3.1 Combined force of two counter propagating red-detuned laser beams vs velocity . . . . . 31

3.2 Scattering rate as a function of the detuning $\Delta$, for different saturation parameters $s_0$ . . . . . 32

3.3 (a)Effects of the light and magnetic fields on the atoms in a MOT. The quadrupole coil magnetic field shifts the energy levels of the atoms. (b) Spatial arrangement of coils and light beams . . . . . 33

3.4 (a)Dark and Bright states in the particular case of the transition $F = 2 \rightarrow F' = 2$ with $\sigma^+$ light. (b) The combined effect of VSCPT and optical pumping to give rise to Gray molasses cooling . . . . . 37

3.5 (a)A gaussian beam travelling along $\vec{z}$ axis is focused and recollimated by a two lenses system. (b) The potential $U_{dip}$ vs $z$ is plotted . . . . . 39

3.6 (Top)The temperature of the dipole trap is obtained through a linear regression as explained in this section. Sizes are plotted versus TOF. (Bottom)Sizes of the cloud for different fall times are outlined . . . . 46

**Chapter 4**

4.1 Scheme of the $^6$Li transitions and light beams used in the experiment 49

4.2 Loading of the MOT (Atom number) vs time . . . . . 51

4.3 Temperature of the MOT measured after compression stage . . . . . 52

4.4 The homebuilt ECDL operating on the $D_1$ line . . . . . 53

4.5 The scheme of the Gray-molasses apparatus and the optical table . . 54

4.6 Atom number of the dipole trap as a function of detuning . . . . . 56

4.7 Breathing-mode radial oscillation trap frequency measurement . . . . 57

4.8 Center of Mass radial oscillation trap frequency measurement . . . . . 58

4.9 The scheme of the feedback system used in our apparatus . . . . . 59

4.10 Comparison between the evaporation ramp as seen on the oscilloscope and the evaporation ramp set on the control system . . . . . 60

4.11 Temperature measurement of the cloud at a trap depth of 18$\mu$K . . . 61

**Chapter 5**

5.1 (a) Hartree interaction. The collision between a condensate particle (straight line) and a thermal leaves the particle unchanged. (b) Fock interaction. The two particles are exchanged after the collision . . . . 65

5.2 Evidence of a bimodal distribution at diferent evaporation stages . . . 68

5.3 Comparison of the fitting between the Semi-Ideal approximation (a) and the Hartree-Fock method (b) . . . . . 71

5.4 Condensate fraction vs Temperature for a fixed interaction strength, $a = 1800a_0$ . . . . . 72

**Abstract**

In this thesis, a stable device for the production of a $^6Li_2$ molecular BEC is presented. Lithium atoms are slowed down by a Zeeman Slower and $10^8$ atoms are trapped in a Magneto Optical Trap. Of these, $\sim 10^6$ atoms are transferred in a red detuned Dipole Trap and an evaporation stage follows, where molecules are formed by tuning interactions via Feshbach resonances. At the end of the evaporation, a condensate containing $\sim 10^4$ molecules is produced.

The condensate is thus analyzed using both the standard Time of Flight technique and the in situ technique, where interactions between the condensate and thermal part are taken into account. In this description, two models are discussed: the semi-ideal approximation and the Hartree-Fock model. The difference between the two models is discussed and supported by experimental data.

Furthermore, the possibility of implementing a Sub-Doppler cooling system for lithium based on the $D_1$ Gray molasses technique is analyzed and a preliminary realization is discussed.

**Acknowledgements**

Over the next few lines I would love to share my gratitude with the people who made my experience in Nottingham unforgettable.

First, I would like to express my deep gratitude to my Master thesis supervisor, Dr. Lucia Hackermueller. She has always been there to help and motivate me, finding a solution to the (many) problems encountered in the lab.

A heartfelt thanks goes to all of the Mixture Lab members. Elisa, Nathan, Vineetha and Pierre, thank you for sharing with me all of the successful, exciting and frustrating moments spent together while working on the different experiments. Thanks also for the stimulating conversations and for introducing me to the challenging world of cold atoms physics.

I would also like to thank the whole Cold atoms group of the University of Nottingham. Thank you for the support you gave me in settling me down in this lovely city, for the interesting and funny discussions, the tasty cakes in the common area and the drinks after work. And after all of this eating and drinking, thank you for the strenuos Badminton and table tennis games.

A sincere gratitude to Liam and his sister Grace, David and all of those interesting people who made my time in Nottingham and generally in England particularly enjoyable out of the University.

I would love to thank Fabio, Manuel and Luciano who took a flight to come here and have a beer with me. I would like to thank my brother Marco who spent some days here, and my youngest brother Matteo, who will visit me in my next adventure.

I must express my deepest gratitude to my parents, for providing me with support and encouragement during all of my years of study, leaving me the freedom of choosing for myself and accepting my (many) mistakes.

Finally, an invaluable thanks goes to my partner Debora. Thank you for supporting me everyday of my life, especially during this year spent in Nottingham. All of our conversations, our trips and experiences are of inestimable value for me.

# Chapter 1

# Introduction

Over the past three decades, our knowledge of the ultracold physics and our ability to cool and trap atoms has improved considerably. In 1985 it was demonstrated by S.Chu at al [1] the first experiment of laser cooling to the Doppler temperature of $240\mu K$, with sodium atoms. Further investigation led to the observation of temperatures below the Doppler limit [2] and to a growing interest in the exploration of the ultracold physics. In 1987 the first Magneto Optical Trap (MOT) was demonstrated [3] and consequently the ability of trapping atoms in addition to reaching very low temperatures.

But why is the ultracold physics gaining so much interest among the scientific world? Firstly, it is undoubtedly a fascinating world, where experimentalists and theorists can work at the frontiers of a new field, studying the nature at extreme scales, so far from common sense. Secondly, ultracold physics is the perfect ground for many-body quantum systems study. Feynman itself proposed in 1982 to use analogous controllable quantum systems to study many-body quantum phenomena [4].

Ultracold atoms have remarkable properties which distinguish them among all the other systems. The possibility of controlling at will most of the experimental parameters makes them the ideal candidates for this purpose. Parameters like interaction [5], dimensionality [6] and trapping potential [7] can all be externally controlled to recreate the desired experimental conditions.

The growing interest and enthusiasm brought to the production of the first Bose-Einstein Condensate (BEC) samples in 1995, with $^{87}$Rb [8], $^{23}$Na [9] and $^{7}$Li [10], all bosonic elements. The first molecular BEC was produced in 2003, using the fermionic $^{7}$Li counterpart, $^{6}$Li [11]. The realization of a molecular condensate from an atomic fermionic element has been made possible thanks to the possibility of controlling interactions between atoms and form a bosonic molecular state, exploiting Feshbach resonances [12]. All the work described in this dissertation has been carried out using $^{6}$Li.

In this Thesis I describe the realization and characterization of a molecular BEC (mBEC) produced from the fermionic Lithium element, $^{6}$Li. When I joined the group in October 2016 the Lithium experiment was not running, as the group was mainly focused on the QUILMI experiment [13]. The pre-existing setup was already capable of producing a molecular BEC, as stated in [14], but it needed an important work to return to a stable condition. Initially, my attention has been dedicated to the optical table and alignment of the optical components, in order to reproduce the ideal laser conditions for the production of a Magneto Optical Trap (MOT). These efforts led to the conditions for a good loading of the Dipole Trap, a fundamental starting point for reaching quantum degeneracy. Thanks to the other members of the group, we were able to trap up to $10^6$ atoms in the dipole trap. From there, a stable production of a mBEC followed. As it will be explained in Chapter 4, there are different methods used to describe a condensate. Interactions play a key role in the production of a condensate, but not all of these methods take into account mutual interactions between the condensate and the thermal part. My focus in this work was to look for evidence of a difference in the description of a condensate using the Semi-Ideal method and the Hartree-Fock method.

This work has been accomplished by a starting construction of a new sub-Doppler cooling method, namely $D_1$ Gray Molasses, and a preliminary study on a new Imag-

ing method, based on Faraday effect.

This Thesis is organized as follows:

- **Chapter 2: Theoretical background**. In this chapter the fundamental theory necessary to understand the experiment is highlighted. A basic description of the properties of Alkali elements is followed by atomic interaction with static magnetic fields and general light and matter interaction. Last part of the chapter is dedicated to Scattering Theory and Feshbach resonances.

- **Chapter 3: Experimental Techniques**. The main experimental techniques used in the experiment are discussed. The principles of laser cooling are explained and a description of how these are implemented in the Zeeman Slower and the Magneto Optical Trap is realized. Hence, it is explained how atoms are trapped in a far red detuned Dipole Trap and evaporatively cooled down to quantum degeneracy. A digression on Imaging techniques follows.

- **Chapter 4: Experimental Apparatus**. The apparatus is described and the characterization of the different stages is reported.

- **Chapter 5: $^6Li_2$ BEC and In situ characterization**. In this chapter the different methods used to characterize a condensate are discussed. Firstly, a simple Ideal gas treatment is analyzed and the Thomas-Fermi approximation is discussed. Secondly, a Semi Ideal model is presented. Thirdly, the Hartree-Fock model and experimental results are presented.

# Chapter 2

# Theoretical background

In this chapter the essential theory behind the experiment is presented, starting from the physical properties of Alkali atoms, fermionic $^6$Li in particular, and their interaction with electric and magnetic fields. This will be followed by an analysis of the interaction between light and matter, which is fundamental in this experiment. The last section of this chapter will be dedicated to scattering theory, in order to better understand collisions in ultracold gases and Feshbach resonances, used extensively to manipulate interactions between atoms.

## 2.1 Properties of Alkali atoms

### 2.1.1 Atomic structure

Laser cooling and trapping exploits the knowledge of physical properties of atoms, it is therefore fundamental to fully understand their structure.

Even if realization and observation of quantum degeneracy has been observed and demonstrated in metastable helium [15], ytterbium [16] and chromium [17], Alkali atoms are typically used in laser cooling experiments. The main common feature of Alkali atoms is an unpaired electron in the $S$ shell of the ground state, which makes them the ideal candidates in cold atoms experiments, given their similarity

with the hydrogen atom. Furthermore, a requirement of laser cooling is that atoms possess closed (or nearly closed) transitions so that they will stay in the cooling cycle, resulting in efficient cooling. Alkalis all satisfy this requirement, and the convenience that these optical transitions lie in a region of the electromagnetic spectrum (from near-infrared to mid-visible) which is easily accessible by non particularly expensive lasers.

Having already mentioned the strong similarity with the hydrogen atom, we set the Hamiltonian problem for an alkali atom very close to the Hamiltonian problem of the hydrogen atom [18], considering that the valence electron is the single optically active electron and the core of filled subshells can be ignored. The Hamiltonian $H_0$ for this problem is :

$$H_0 = \frac{\mathbf{p}^2}{2m} + V_{\text{eff}}(\mathbf{r})$$

with $\mathbf{p}$ being the momentum of the electron, $m$ its mass and $V_{\text{eff}} = \dfrac{-Ze^2}{4\pi\epsilon_0 r}$ the effective potential. The solution to this problem is the product between a radial function and an angular function and a good set of quantum numbers is given by $|n, l, m_l\rangle$. The principal quantum number is $n$ and arises from solving the radial equation, while the azimuthal number $l$ and the magnetic number $m_l$ result from angular equations. Unlike in the hydrogen atom, the energy levels for an alkali atom depend on the principal and azimuthal number, because the outer valence electron no longer experiences a pure Coulomb potential, breaking the degeneracy.

This description is intended as a simple introduction to the problem and does not take into account relativistic effects and spin-orbit coupling, which play instead a crucial role for our experiment. The Hamiltonian $H_0$ is just the leading term in the relativistic treatment in the Dirac theory. In this context it is fundamental to consider the electron as a relativistic particle, so we have to make a correction to the kinetic term of the Hamiltonian and we have to consider the interaction between its spin and its orbital angular momentum. The last correction term is the Darwin term, whose correction is important only when the azimuthal number $l = 0$. All of

these three corrections are of the order of $\alpha^2 = (\frac{1}{137})^2$, being $\alpha$ the fine structure constant. The corrected Hamiltonian is now:

$$H = H_0 + mc^2 - \frac{\mathbf{p}^4}{8m^3c^2} + \frac{1}{2m^2c^2}\frac{1}{r}\frac{dV_{\text{eff}}}{dr}(r)\mathbf{L}\cdot\mathbf{S} + \frac{(\hbar)^2}{8m^2c^2}\Delta V_{\text{eff}}(r)$$

The eigenstates of this Hamiltonian can be expressed in the basis $|n, l, s, j, j_z\rangle$, having introduced the operator total angular momentum $\mathbf{J} = \mathbf{L}+\mathbf{S}$ and its projection along $\hat{z}$, $\mathbf{J}_z$. In this basis we can express the spin-orbit coupling term $\mathbf{L}\cdot\mathbf{S} = \frac{1}{2}(\mathbf{J}^2-\mathbf{L}^2-\mathbf{S}^2)$ and the energy correction produced by this coupling is given by:

$$\begin{aligned}
\mathbf{L}\cdot\mathbf{S}\,|n,l,s,j,j_z\rangle &= \frac{1}{2}(\mathbf{J}^2 - \mathbf{L}^2 - \mathbf{S}^2)\,|n,l,s,j,j_z\rangle \\
&= \frac{\hbar^2}{2}\left(j(j+1) - l(l+1) - \frac{3}{4}\right)|n,l,s,j,j_z\rangle \\
&= \frac{\hbar^2}{2}\times\begin{cases}(j-\frac{1}{2})\,|n,l,s,j,j_z\rangle & (j = l+\frac{1}{2}) \\ (-j-\frac{3}{2})\,|n,l,s,j,j_z\rangle & (j = l-\frac{1}{2})\end{cases}
\end{aligned} \tag{2.1}$$

Since $j$ can assume both values $j = l + \frac{1}{2}$ and $j = l - \frac{1}{2}$, we will have a splitting of the energy levels due to the coupling between spin and orbital angular momentum, for values of $l \neq 0$. This is the origin of the so called spin-orbit doublet.
Finally, a proton has a magnetic moment $\mathbf{M} = g_P\frac{e}{2M_P}\mathbf{I}$, with $M_P$ being its mass, $g_P$ its gyromagnetic ratio, and $\mathbf{I}$ its spin vector. This magnetic moment generates a vector potential and a magnetic field and as a result, we obtain interaction with the orbital and spinorial degrees of freedom of the electron. This causes the hyperfine splitting of the energy levels. The interaction Hamiltonian can be expressed as:

$$H_{hfs} = A_{hfs}\mathbf{I}\cdot\mathbf{J} \tag{2.2}$$

The correction produced by $H_{hfs}$ is smaller than fine structure corrections of a factor $\approx 10^{-3}$, being the ration between electron and nuclear mass $\frac{m}{M_N} \approx 10^{-3}$.

Proceeding in analogy with the electron spin-orbit coupling, thus defining a total angular momentum operator $\mathbf{F} = \mathbf{J} + \mathbf{I}$, we can express the eigenstates in term of the basis $|n, l, s, j, i, f, m_f\rangle$. The energy levels will now depend on all the quantum numbers, with the exception of the magnetic number $m_f$. The hyperfine splitting will produce, as we will see later, a doublet in the ground state.

### Lithium

Lithium, in its solid form, is the lightest of all the alkali atoms under standard temperature and pressure conditions and presents a silver-white appearance. Its atomic number is $Z = 3$ and its chemical symbol is Li. Lithium naturally appears in two stable isotopes, $^7$Li with four neutrons, and $^6$Li with three. Since the two isotopes differ by a single spin-1/2 particle, they exhibit different quantum statistics. $^7$Li is hence a boson, while $^6$Li is a fermion. This thesis is based on the work done using the fermionic element, $^6$Li.

| Property | Symbol | Value |
|---|---|---|
| Atomic Number | $Z$ | 3 |
| Natural Abundance | $\eta$ | 7.6% |
| Nuclear Lifetime | $\tau_n$ | stable |
| Total Electronic Spin | $S$ | $1/2$ |
| Total Nuclear Spin | $I$ | 1 |
| Wavelength (vacuum), D2 line | $\lambda$ | 670.992 477 nm |
| Natural Linewidth, D2 line | $\Gamma$ | $36.898 \times 10^6$ s $^{-1}$<br>5.872 4 MHz |

*Table 2.1: Fundamental physical properties of atomic Li [19].*

Being an Alkali atom, Lithium has a single outer valence electron and its ground state configuration is $1s^2 2s^1$, while the excited state configuration is $1s^2 2p^1$. Historically indicated as the Fraunhofer D-line is the transition between the ground and the excited states, which exhibits two sub-features, the $D_1$ and $D_2$ lines, created

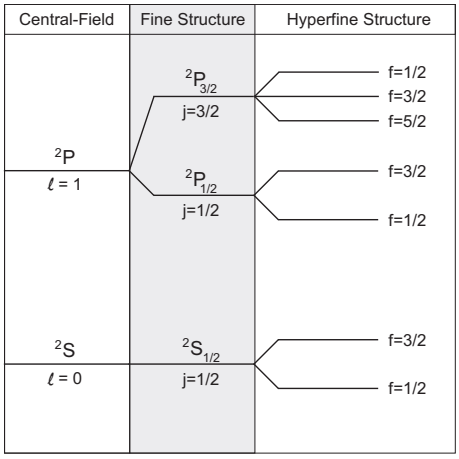



*Figure 2.1: The figure shows the energy splittings of the ground end excited states, and the relative fine and hyperfine structure. The states are expressed in spectroscopic notation and the splitting is not to scale.*

by the spin-orbit coupling, as described in the previous section. The linewidth $\Gamma$ is inversely related to the excited state lifetime :

$$\Gamma = \frac{1}{\tau} \tag{2.3}$$

and for Lithium this is the same for both the $D_1$ and $D_2$ lines. This is a peculiarity, while it differs instead for other Alkali atoms, since the difference between the two linewidths relies within uncertainty of the most precise measurement done at the writing of this thesis [20].

As mentioned previously, laser cooling requires a closed optical loop in which to cycle the atoms. The level structure of the $D_2$ line is typically exploited for this task with lithium. Advantageously, the $D_2$ line is in the red visible spectrum at 671 but unfortunately the $^2P_{3/2}$ excited state of this transition has an unresolved hyperfine structure , hence not allowing us to reach sub doppler cooling. Typical magneto-optical trap (MOT) temperatures for lithium are therefore $\approx 300\mu K$.

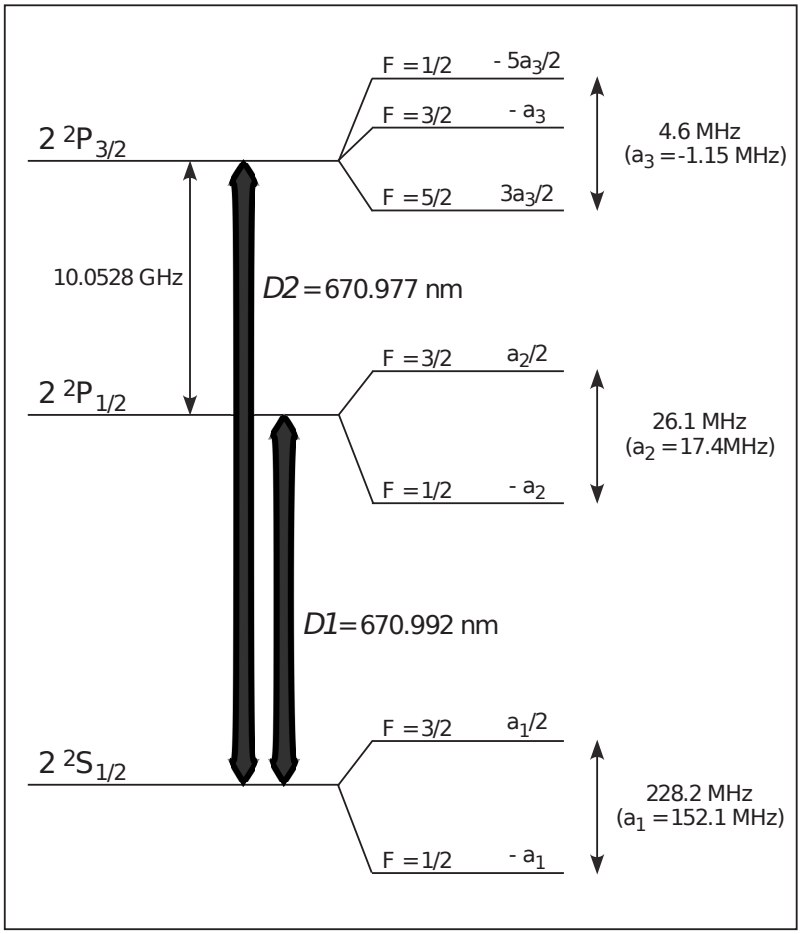



*Figure 2.2: The figure shows $D_1$ and $D_2$ Li lines with relative wavelenghts. Splittings not to scale.*

## 2.2 Interaction with static magnetic fields

When describing the physical properties of atoms, we have underlined the importance of the presence of intrinsic magnetic moments of the atom itself. We distinguished between a magnetic dipole moment $\mu_L$ given by the orbital angular momentum $L$, an intrinsic spin magnetic moment $\mu_S$ given by the intrinsic spin vector $S$ and a nuclear momentum $\mu_I$, arising from the spin of protons and neutrons in the nucleus. We described how these quantities interact with each other, producing modifications in the energy structure of the atom itself. Given the magnetic nature of this quantities, it is legit to expect interaction with external magnetic fields. Magnetic fields are extensively used in atomic physics and in cold atoms experiments, because of their peculiarity of modifying the energy structure of atoms, manipulating them according to the experiment needs. Many instruments and physical tools in our experiment exploit the knowledge we have about the interaction between static magnetic fields and atoms. The Zeeman slower, the Magneto-optical trap and the Feshbach resonances are the most important examples. It is hence fundamental to understand the process of this interaction.

The total Hamiltonian of an atom in an external magnetic field is $H = H_0 + V_M$, where $H_0$ is the unperturbed Hamiltonian and $V_M$ is the term due to the magnetic field:

$$V_M = \frac{\mu_B}{\hbar}(g_S\mathbf{S} + g_L\mathbf{L} + g_I\mathbf{I})\mathbf{B} \tag{2.4}$$

where $\mu_B$ is the Bohr magneton and the $g_{S,L,I}$ are the gyromagnetic ratios of the atom. In resolving this problem, we have to compare the interaction strength of the external applied field and the hyperfine interaction *with* the interaction strength of the hyperfine structure. We can hence define three different regimes :

- Low field: when the interaction of the external field and the hyperfine structure is small compared to the hyperfine structure interaction and hence treated treated like a perturbation

- High field: when the interaction of the external field and the hyperfine structure is dominant compared to the hyperfine structure interaction and hence we treat we treat the hyperfine structure like a perturbation

- Intermediate regime : when the two interaction terms are comparable and perturbation theory is no longer applicable. In this case we have to solve the hamiltonian problem.

At low field, $F$ and $m_F$ are good quantum numbers and the energy shift with respect to the magnetic field strength is given by [18]:

$$E = g_F \mu_B m_F B \tag{2.5}$$

with the Landè factor being:

$$g_F = \frac{F(F+1) + J(J+1) - I(I+1)}{2F(F+1)} g_J \tag{2.6}$$

In the high field regime, also known as the Paschen-Back regime, F is no longer a good quantum number. The electrons total angular momentum J and the nuclear angular momentum I couple directly to the external field and we can treat the hyperfine structure like a perturbation. The energy splitting is given by [18]:

$$E = g_J \mu_B m_J B + A m_I m_J \tag{2.7}$$

where A is the magnetic dipole constant for a given level.
In the intermediate regime, the solution to the Hamiltonian problem is not as direct as it is in the low or high field regime, but the energy shifts can be computationally evaluated.
In this Section, we have explained atomic structure and electronic levels that would be addressed with photons. A discussion on light-matter interaction models will follow in the next one.

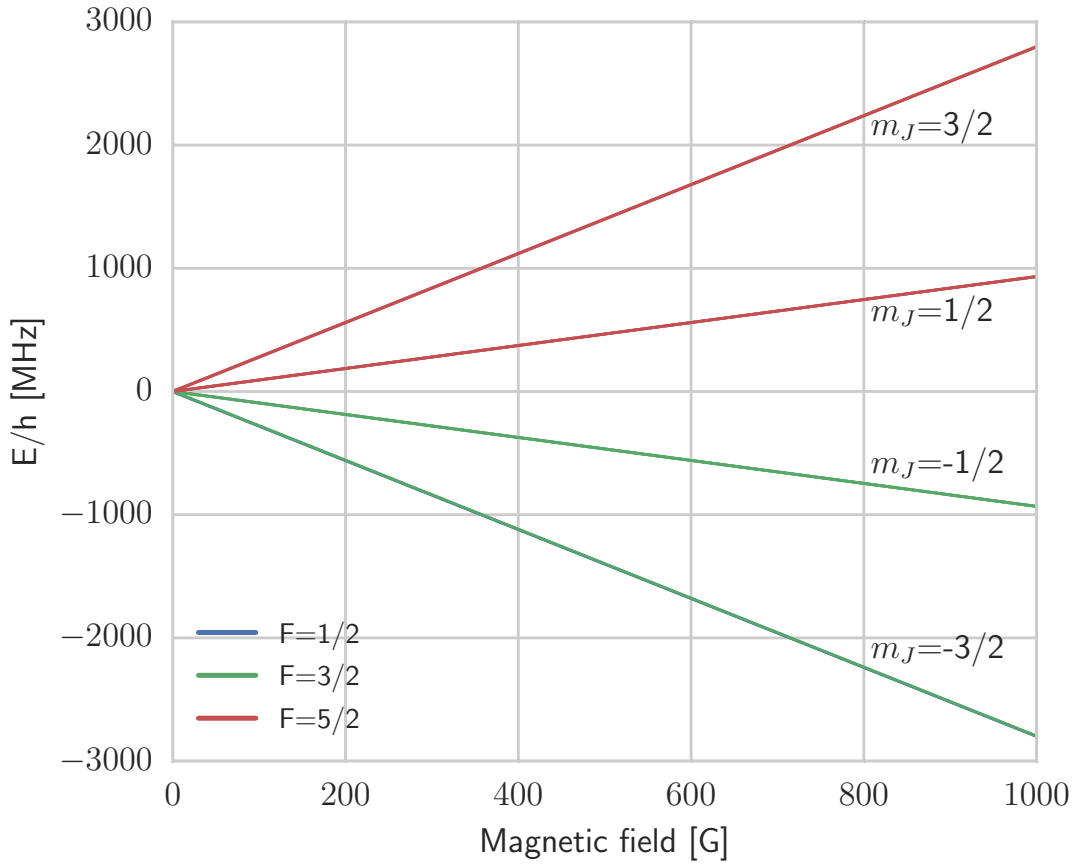



*Figure 2.3: Calculated Breit-Rabi diagram of the $^6Li\ ^2P_{3/2}$ manifold*

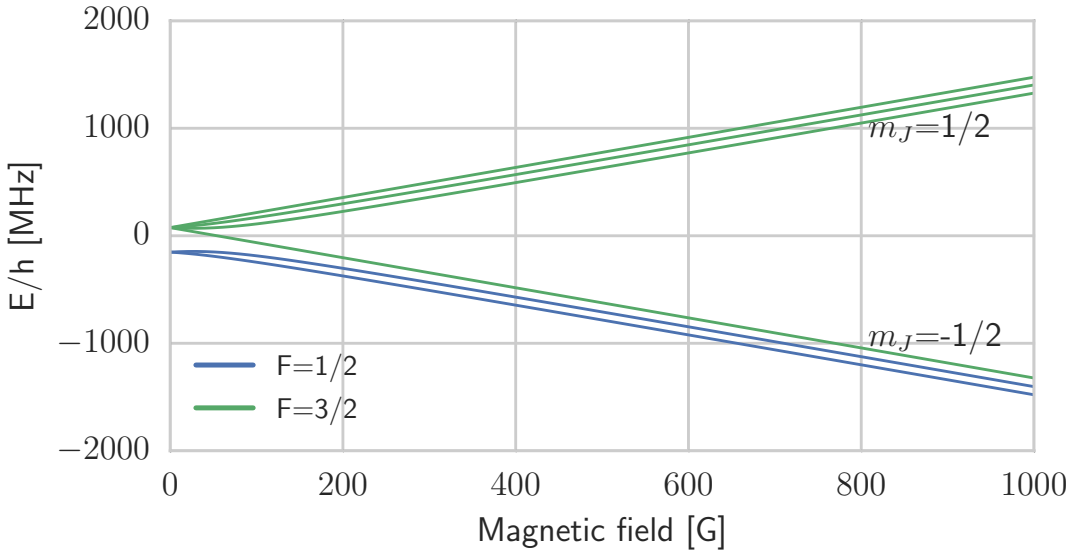



*Figure 2.4: Calculated Breit-Rabi diagram of the $^6Li\ ^2S_{1/2}$ manifold*

## 2.3 Light and Matter interaction

Interaction between light and matter is a fundametal process in modern physics and allows us in particular to achieve atom cooling and trapping. We can approach the problem of the interaction between light and matter in a semi-classical way, describing the atoms as a two-level quantum system in a radiation field, which is instead classically treated.

In the presence of an external field $\mathbf{E} = \mathbf{E}\cos(\omega t)$, the atom has an induced dipole moment $\mathbf{p} = \alpha\mathbf{E}$, with $\alpha$ being the complex polarizability [21].

The interaction potential of the induced dipole moment $\mathbf{p}$ in the driving field $\mathbf{E}$ is given by:

$$U_{\text{dip}} = -\frac{1}{2}\langle \mathbf{pE} \rangle = -\frac{1}{2\epsilon_0 c}\,\text{Re}(\alpha) I \tag{2.8}$$

where $\frac{1}{2}$ takes into account that the dipole is induced and not permanent, the angular brackets indicate a time average on the rapid oscillations and $I = 2\epsilon_0 c|\mathbf{E}^2|$ is the laser intensity. The potential energy of the atom in the field is thus proportional to the intensity $I$ and to the real part of the polarizability, which describes the in-phase

component of the dipole oscillation being responsible for the dispersive properties of the interaction. The dipole force results from the gradient of the interaction potential:

$$\mathbf{F}_{\mathrm{dip}}(\mathbf{r}) = -\nabla U_{\mathrm{dip}}(\mathbf{r}) - \frac{1}{2\epsilon_0 c}\,\mathrm{Re}(\alpha)\nabla I(\mathbf{r}) \tag{2.9}$$

This is thus a conservative force, depending on the gradient field of the laser intensity. The power absorption is instead given by :

$$P_{\mathrm{abs}} = \langle \dot{\mathbf{p}}\mathbf{E} \rangle = 2\omega\,\mathrm{Im}(\mathbf{p}\mathbf{E}^*) = \frac{\omega}{\epsilon_0 c}\,\mathrm{Im}(\alpha) I \tag{2.10}$$

The absorption is related to the imaginary part of the polarizability, describing the out-of-phase component of the dipole oscillation. We can explain the photon absorption in terms of photon scattering in cycles of absorption and emission processes, defining the scattering rate as the power absorption divided by the energy of single photon:

$$\Gamma_{\mathrm{sc}}(\mathbf{r}) = \frac{P_{\mathrm{abs}}}{\hbar\omega} = \frac{1}{\hbar\epsilon_0 c}\,\mathrm{Im}(\alpha) I(\mathbf{r}) \tag{2.11}$$

In our semiclassical approach, we can explicitly derive the above quantities for a two level atom, away from resonance and neglecting excited state saturation. To perform this calculation, we use the polarizability obtained from Lorentz's model of the atom as a classical oscillator, with an oscillation frequency $\omega_0$, corresponding to the optical transition. In this model damping is introduced, which corresponds classically to the radiation emitted by the oscillating electron, substituted in our approach by the decay rate $\Gamma$ give by the dipole matrix element between ground and excited state:

$$\Gamma = \frac{(\omega_0)^3}{3\pi\epsilon_0\hbar c^3} |\langle e|\,\mathbf{p}\,|g\rangle|^2 \tag{2.12}$$

The two level model quantities $U_{\mathrm{dip}}$ and $\Gamma_{\mathrm{sc}}$ are :

$$U_{\mathrm{dip}}(\mathbf{r}) = -\frac{3\pi c^2 \Gamma}{2{\omega_0}^3}\left(\frac{1}{\omega_0 - \omega_L} + \frac{1}{\omega_0 + \omega_L}\right) I(\mathbf{r}) \tag{2.13}$$

$$\Gamma_{\rm sc}(\mathbf{r}) = \frac{3\pi c^2 \Gamma^2}{2\hbar {\omega_0}^3}\left(\frac{\omega_L}{\omega_0}\right)^3\left(\frac{1}{\omega_0-\omega_L}+\frac{1}{\omega_0+\omega_L}\right)^2 I(\mathbf{r}) \tag{2.14}$$

These quantities are valid for any driving frequency and they exhibit a resonant behaviour for $\omega = \omega_0$ and for $\omega = -\omega_0$. Adopting the *rotating-wave-approximation*, which is of practical interest in many experiments where laser frequency is relatively close to resonance, we can write $U_{\rm dip}$ and $\Gamma_{\rm sc}$ as follows:

$$U_{\rm dip}(\mathbf{r}) = \frac{3\pi c^2}{2{\omega_0}^3}\frac{\Gamma}{\Delta} I(\mathbf{r}) \tag{2.15}$$

$$\Gamma_{\rm sc}(\mathbf{r}) = \frac{3\pi c^2}{2\hbar {\omega_0}^3}\left(\frac{\Gamma}{\Delta}\right)^2 I(\mathbf{r}) \tag{2.16}$$

having introduced the detuning $\Delta = \omega - \omega_0$ and neglected the counter rotating term.

From the previous expressions we will be able to explain the principles behind laser cooling and trapping, that we are going to explain more in detail in chapter 3. These notions will be fundamental for our experiment, as we will see in chapter 4.

## 2.4 Scattering Theory

In achieving quantum degeneracy collisions play a key role, for example they are essential during the evaporative cooling phase and in the creation of the Feshbach molecules. So far, single atom properties have been discussed and an overview of scattering theory is essential at this point.
The collision between two particles can be described in the center of mass reference frame. The Hamiltonian for this system is:

$$H = \frac{\mathbf{P}^2}{4m} + \frac{\mathbf{p}^2}{m} + V(\mathbf{r}) \tag{2.17}$$

The first term of the Hamiltonian describes the center of mass of the system, which behaves as a free particle of momentum $\mathbf{P} = \mathbf{p}_1 + \mathbf{p}_2$, being $\mathbf{p}_1$ and $\mathbf{p}_2$ the momenta

of the colliding particles. The last two term characterise the scattering process, described by a relative particle of momentum $\mathbf{p} = (\mathbf{p}_1 - \mathbf{p}_2)/2$ and a potential $V(\mathbf{r}) = V(\mathbf{r}_1 - \mathbf{r}_2)$. Far from the scattering centre, the general solution for this problem is:

$$\psi_k(\mathbf{r}) \approx e^{i\mathbf{k}\cdot\mathbf{r}} + f_k(\theta)\frac{e^{ikr}}{r} \tag{2.18}$$

with $\mathbf{k}$ being the wavevector of the scattered wave with magnitude $k = (2m_r{}^1E/\hbar)^{1/2}$. This solution has the form of an incoming plane wave and an outgoing spherical wave with an angular distribution defined by the scattering amplitude $f_k(\theta)$. The scattering amplitude is particularly relevant because it is directly related to the scattering cross section, which is a measurable quantity. The differential scattering cross section is defined as the number of particles within an infinitesimal area $d\sigma$, that scatter into an infinitesimal solid angle $d\Omega$. In the case of distinguishable particle, this relation is:

$$\frac{d\sigma}{d\Omega} = |f_k(\theta)|^2 \tag{2.19}$$

For a central scattering potential, the radial and angular parts of the Schrödinger equation can be solved separately and the general solution can be expressed in the form [22]

$$\psi(r, \theta, \phi) = R(r)Y_l^m(\theta, \phi) \tag{2.20}$$

$Y_l^m(\theta, \phi)$ denotes the spherical harmonic functions and $R(r)$ satisfies the radial Schrödinger equation:

$$\left[-\frac{\hbar^2}{2m_r}\frac{d^2}{dr^2} + \frac{\hbar^2}{2m_r}\frac{l(l+1)}{r^2} + V(r)\right] rR_l(r) = ErR_l(r) \tag{2.21}$$

where an effective potential

$$V_{\text{eff}} = \frac{\hbar^2}{2m_r}\frac{l(l+1)}{r^2} + V(r) \tag{2.22}$$

[1] $m_r$ is the reduced mass $m^2/(m+m) = m/2$ in this case

is considered, Fig.2.5. For a central potential $\psi(r, \theta, \phi)$ does not depend on $\phi$ and the spherical harmonic functions are of the form:

$$Y_l^0 = \sqrt{\frac{2l+1}{4\pi}} P_l(\cos\theta) \tag{2.23}$$

where $P_l$ is the $l^{th}$ Legendre polynomial. The scattering amplitude is thus determined by comparing the general solution of the Schrödinger equation with the ansatz given in Eq.(2.18). From this we obtain:

$$\psi_k(\theta) = \sum_{l=0}^{\infty} (2l+1) f_l P_l(\cos\theta) \tag{2.24}$$

where $f_l$ is called the partial wave amplitude of the $l^{th}$ partial wave. Each partial wave induces a phase shift $\delta_l$ to the scattered wave and $f_l$ can be written in terms of $\delta_l$ as $f_l = (e^{i\delta_l} \sin\delta_l)/k$. The total cross section $\delta$ can be obtained integrating over all solid angles:

$$\sigma(k, \delta_l) = \frac{4\pi}{k^2} \sum_{l=0}^{\infty} (2l+1) \sin^2(\delta_l) \tag{2.25}$$

When we derived this result, we assumed the particles to be distinguishable. In the case of identical particles, the right simmetry conditions must be explicitated:

$$\sigma(k, \delta_l) = \frac{8\pi}{k^2} \sum_{even\ l}^{\infty} (2l+1) \sin^2(\delta_l) \qquad \text{Bosons} \tag{2.26}$$

$$\sigma(k, \delta_l) = \frac{8\pi}{k^2} \sum_{odd\ l}^{\infty} (2l+1) \sin^2(\delta_l) \qquad \text{Fermions} \tag{2.27}$$

If we look back at the $V_{\text{eff}}$ in Eq.(2.22), we note it is the sum of $V(r)$ and a centrifugal term, depending on $l$. For partial waves with angular momentum $l > 0$, there is a centrifugal barrier to the potential, with important consequences in the specific case of low energies. In this ultracold regime the collision energy $E_k$ is so small that the centrifugal barrier effectively blocks all the partial waves with

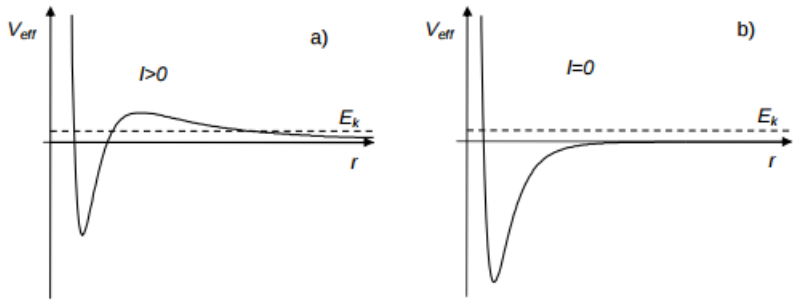



*Figure 2.5: Effective potential $V_{\text{eff}}$ for the radial part of the partial waves. (a) A centrifugal barrier inhibits collisions for low energies, in the case of $l > 0$. (b) The absence of the centrifugal barrier for the s-wave ($l = 0$) allows collisions for very low energies.*

$l > 0$ from the region where the potential considerably differs from 0, Fig 2.5. As a consequence, only s-waves ($l = 0$) contribute to the scattering of ultracold atoms. This scattering threshold can be calculated and, in terms of temperature, is equal to 8mK for Lithium [23].

Thus, for bosons, the contribution to the cross section $\sigma$ is only given by the s-wave and it approaches a constant value:

$$\sigma_{l=0}(k) \longrightarrow 8\pi a_0^2 \tag{2.28}$$

with $a_0$ being the s-wave scattering length:

$$a_0 = -\lim_{k\to 0} \frac{\tan(\delta_0(k))}{k} \tag{2.29}$$

### 2.4.1 Feshbach resonance

An essential tool for the study of cold and ultracold gases is the use of the Feshbach resonances. Through an external magnetic field is in fact possible to tune the scattering length $a$, which rules the strength of interatomic interactions and whether they are repulsive or attractive [24].

A Feshbach resonance occurs when the kinetic energy of two particles colliding in an open-channel, matches the energy of a bound molecular state in a closed channel.

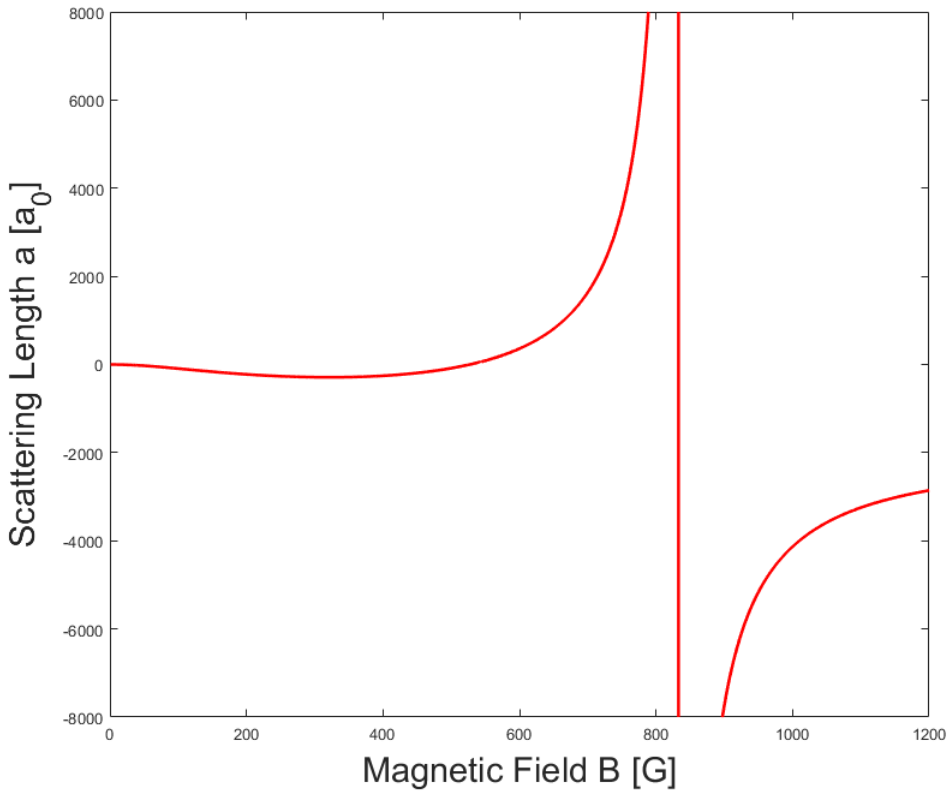



*Figure 2.6: Scattering length as a function of magnetic field for $^6Li$ atoms in the lowest ground state. The s-wave resonance is located at 832.18 G. Data taken from [25]*

The interaction legth $a$ can be expressed as a function of the magnetic field B:

$$a(B) = a_{\mathrm{BG}} \left(1 - \frac{\Delta}{B - B_0}\right) \tag{2.30}$$

where $a_{BG}$ is the non-resonant s-wave scattering length known as the background scattering length, $\Delta$ is the width of the resonance and $B_0$ is the field value where the resonance occurs. Interactions can be tuned on either side of the resonance and it is thus possible to make them attractive ($a < 0$) or repulsive ($a > 0$), Fig.2.6.
In the BEC limit, the molecule-molecule scattering length to be used is $0.6a$, $a$ being the atomic scattering length.

# Chapter 3

# Experimental Techniques

While in chapter 2 we have discussed the fundamental principles necessary to understand the experiment, in this chapter we are going to explain how they are experimentally implemented in our lab in order to produce a Bose-Einstein condensate. Following the storyline mentioned in the Introduction, we will see how an atomic beam is slowed down using a Zeeman Slower and how an atomic cloud is cooled down and trapped in a MOT. Furthermore, since the phase-space density in the MOT is not sufficient to reach quantum degeneracy [26], further cooling is required. This is how a red detuned dipole trap is introduced and evaporative cooling is discussed as the final step towards the BEC production. Finally, emphasis will be on imaging, an indispensable tool when investigating the properties of an ultracold cloud.

## 3.1 Laser Cooling

### 3.1.1 Scattering Force

From the previous notions of the interaction between light and matter discussed in chapter 2, we can understand and explain how we can achieve laser cooling of an atomic cloud. Due to the dissipative nature of the scattering force $F_{\text{sc}}$, we can exploit its properties and cool down an atom over many cycles of absorption and

spontaneous emission.

As we previously saw in Section 2.3, we can describe the absorption and the emission of photons in terms of a quantity called *scattering rate* $\Gamma_{\rm sc}$, which is defined as the ratio between the power absorbed and the energy of the single photon. By multiplying the scattering rate $\Gamma_{\rm sc}$ by the photon momentum $\hbar\mathbf{k}$, we obtain the scattering force $F_{\rm sc}$, which can be exploited in the following technique.

Consider a two-level atom system. The technique is based on the recoil kick an atom experiences when it absorbs a photon from a counter-propagating laser beam. The excited atom later decays via spontaneous emission and thus receives another momentum kick. Since the photons spontaneous emission can occur randomly in any direction, if we average over many absoprtion-amission cycles we'll obtain that the second momentum kick goes to zero. Thus on average, for each cycle the atom receives a momentum kick of $\hbar\mathbf{k}$, where $\mathbf{k}$ is the laser wavevector. It is reasonable to expect that the scattering rate is maximised on resonance ($\Delta = 0$), however the natural linewidth of the excited state implies scattering can still occur off-resonance. The equation 2.14 does not take into account the excited state saturation, which we obtain from the *Optical Bloch Equations*. Introducing the saturation parameter $s = \dfrac{I(\mathbf{r})}{I_{\rm sat}}$, we can express the scattering rate as:

$$\Gamma_{\rm sc}(\mathbf{r}) = \frac{\Gamma}{2}\frac{s}{1 + s + 4^{\Delta^2}/_{\Gamma^2}} \tag{3.1}$$

The saturation intensity $I_{sat}$ is given by $I_{sat} = \dfrac{2\pi^2\hbar\Gamma c}{3\lambda^3}$. For the $D_2$ line of a $^6$Li atom ($\lambda = 670.977nm$), with a natural linewidth of $2\pi * 5.874$MHz, the saturation intensity $I_{sat}(D_2)$ is 2.84mW/cm$^2$.

To understand how we can slow down an atom using laser cooling, we describe a situation unidimensional in which an atom travels among two counter-propagating beams [27]. We know that the frequency of the laser that the atom experiences depends on its own velocity and it is shifted of a quantity $\mathbf{k}\cdot\mathbf{v}$, called Doppler shift.

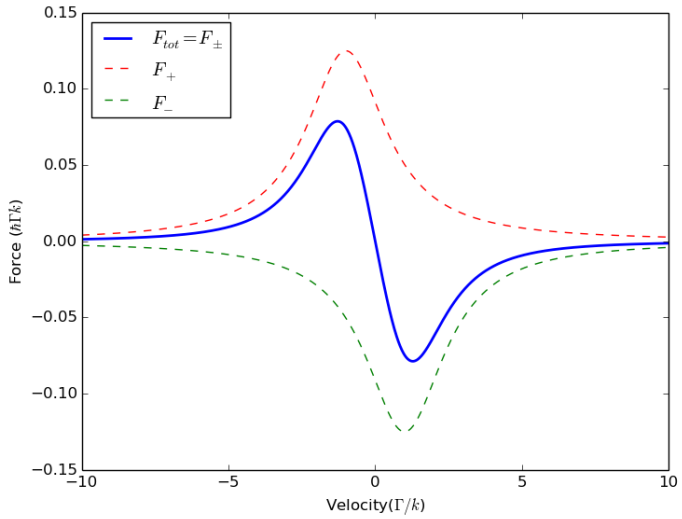



*Figure 3.1: The figure shows the combined force of two counter propagating red-detuned laser beams vs velocity. The red dashed line is $F_+$, the green dashed line is $F_-$, and the solid line is the total force $F_\pm$. The parameters used to produce the plot were $s_0$ = 0.1 and $\Delta/\Gamma$ = -0.3*

We can implement the Doppler shift in the scattering rate by replacing the detuning $\Delta \to \Delta + \mathbf{k}\cdot\mathbf{v}$. At this point we can derive the scattering force by multiplying the scattering rate $\Gamma_{sc}$ by the momentum of each scattered photon $\hbar\mathbf{k}$. In our situation of two counterpropagating beams, the atom will experience a force which is the sum of the force exerted by the two beams: $\mathbf{F} = \mathbf{F}_+ + \mathbf{F}_-$, where the individual contributions $\mathbf{F}_\pm$ are :

$$\mathbf{F}_\pm = \pm\frac{\hbar k\Gamma}{2}\frac{s}{1+2s+4^{(\Delta\mp kv)^2}/\Gamma^2} \tag{3.2}$$

Atoms experiencing instead a single counter propagating beam will be slowed down. This is exploited in the Zeeman Slower, which is the first step of our experiment.

### 3.1.2 Zeeman slower

In our experiment, an atomic flux of Lithium is produced from an oven at a temperature greater than 400°C, where the most probable velocity of the atoms is 1400m/s.

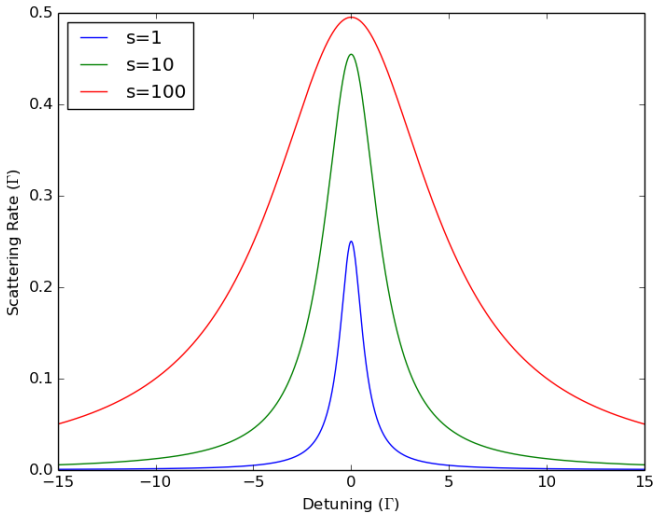



*Figure 3.2: Scattering rate as a function of the detuning $\Delta$, for different saturation parameters $s_0$*

In order to be captured in our Magneto Optical Trap, an atom needs to be slowed down to a velocity of 230m/s. We previously saw how the force experienced by an atom under many cycles of absorption and emission can slow it down. The assumption of this technique is that, in order to maximize the absorption probability, the light shone is always resonant with the atomic transition. The arising problem in this context is that when a moving atom changes its velocity, then its Doppler shift changes, so the atom *sees* a different frequency and the light is not resonant anymore. A common technique used to effectively cool down an atomic beam consists in using a magnetic field with a varying profile so that atoms are always resonant with the light, because of the shifts of the atomic levels due to the Zeeman effect. This technique was developed by William Phillips and Harold Metcalf, [28].
Including the effect of the magnetic field, the total detuning becomes:

$$\Delta = \Delta_0 + kv(z) \pm \frac{\mu}{\hbar} B(z) \tag{3.3}$$

where $\Delta_0$ is the laser detuning from the atomic transition, $kv(z)$ is the Doppler shift term and the sign $\pm$ is determined by the light polarization. For an effective cooling,

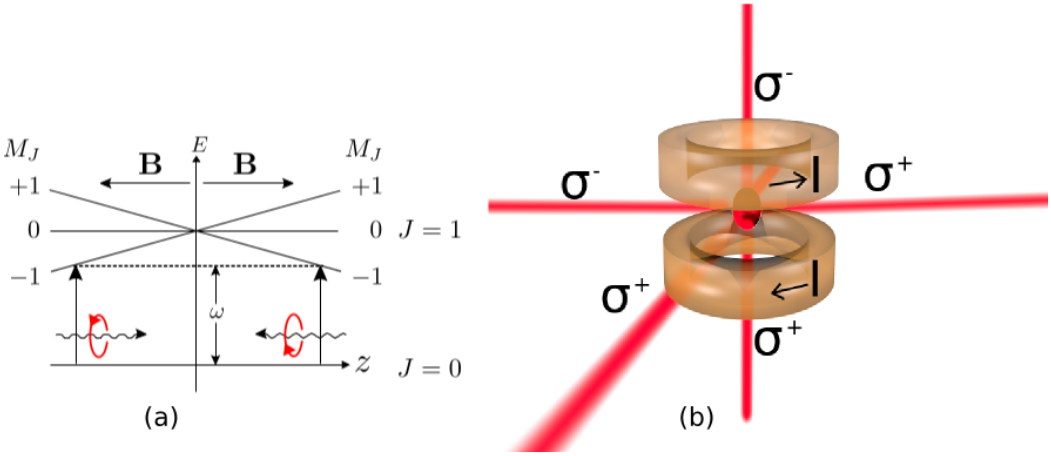



*Figure 3.3: (a)Effects of the light and magnetic fields on the atoms in a MOT. The quadrupole coil magnetic field shifts the energy levels of the atoms. Polarized light pushes them towards the center of the trap. (b) Spatial arrangement of coils and light beams*

we want the total detuning to be always $\Delta = 0$. In order to obtain this, we need to build an efficient magnetic field profile. If we assume a constant deceleration, we can express $v(z)$ as follows:

$$v(z) = \sqrt{{v_0}^2 + 2v_0 z} \tag{3.4}$$

Substituting (3.4) in Eq.(3.3) and expressing in term of $B(z)$:

$$B(z) = \frac{\hbar}{\mu}\left(\Delta + k\sqrt{{v_0}^2 + 2v_0 z}\right) \tag{3.5}$$

where we can obtain $a_0$ from the scattering force:

$$a_0 = \frac{F_{\text{sc}}}{m} = \frac{\Gamma}{2m}\hbar k\frac{s}{1+s} \tag{3.6}$$

## 3.2 The Magneto Optical Trap

After leaving the Zeeman Slower, atoms are trapped in a Magneto Optical Trap. During this stage, atoms are furtherly cooled down and with the help of the magnetic

field they are spatially confined. As previously seen light exerts a dissipative force, being the atoms immersed in two counterpropagating beams, while the presence of a magnetic field gradient modifies the internal structure of the energy levels, keeping the atoms spatially confined.

In order to understand how it is possible to trap the atoms, we first consider a 1-Dimension situation with two counter propagating beams and a $J = 0 \Rightarrow J = 1$ transition, as shown in Fig. 3.3(a)

The magnetic field is produced by two coils in anti-Helmoltz configuration, which produce a quadrupole magnetic field with a zero field region at the center. When an atom is placed in this region, its internal structure will not be affected and no variation in its energy levels will appear. As the atom travels away from the center, because of the presence of the magnetic field, it will experience a modification of its energy levels, in particular the energy sublevel $M_J = -1$ will be red-shifted respect the magnetic sublevel $M_J = +1$ in this case. Since the light in the two beams is red shifted, the atom will be more resonant with the counter propagating beam having polarization $\sigma^+$, pushing it again towards the center of the magnetic field. On the other hand, when the atom travels in the opposite direction, the situation is reversed but the atom will always be pushed towards the centre of magnetic field region. Expanding this to a 3-D situation with three pairs of counterpropagating beams, we obtain a spatially confined trap.

### 3.2.1 The Doppler limit

In this section we are going to discuss the existence of a limit to the temperature achievable through the cooling mechanism explained so far. When an atom undergoes many cycles of absorption and emission, as well as the cooling deriving from the scattering force, heating naturally occurs. From each event of absorption or emission, the atom gains a kinetic energy term due to the photon recoil. In fact, its

momenutm changes of $\hbar k$ for each event, increasing its energy of a term $E_r = \frac{\hbar^2 k^2}{2m}$, leading to heating.

Equating the cooling and heating processes, we can derive the temperature limit [18]:

$$k_B T = \frac{\hbar\Gamma}{4} \frac{1 + (2\Delta/\Gamma)^2}{-2\Delta/\Gamma} \tag{3.7}$$

where $T$ is the temperature, $\Delta$ is the detuning from resonance and $\Gamma$ is the linewidth of the atomic transition. This function shows a minimum for a detuning value of $\Delta = -\Gamma/2$, leading to a theorethical temperature value of:

$$k_B T_D = \hbar\frac{\Gamma}{2} \tag{3.8}$$

where $T_D$ is the Doppler limit. The Doppler limit for $^6$Li is $140\mu K$, using the $D_2$ line transition.

### 3.2.2 Prospects on Sub-Doppler Cooling

From the previous sections we know that temperatures below the Doppler limit cannot be achieved in a MOT. One of my tasks during my time spent here in Nottingham was to investigate the possibility of implementing a sub-Doppler cooling method to our apparatus. After investigating some different methods and studying their practical realization, I concluded that a Gray molasses technique on the $D_1$ line cooling transition could be implementable in our setup without too much effort, following the example of [29].

The Gray molasses technique exploits a Sisyphus-like effect for reaching sub-Doppler cooling, thanks to the creation of bright and dark states and the coupling between them given by VSCPT, velocity-selective coherent population trapping [30], [31], [29].

Necessarily we need to implement this technique on the $D_1$ line, because we want the creation of bright and dark states and this can only happen for transitions in which

$F \to F' = F$ or $F \to F' = F - 1$ [32]. In this condition, for any polarization state of the local electromagnetic field, there exists a magnetic sub-level of the ground state which is not coupled to any of the magnetic sub-levels of the excited state, see Fig. 3.4(a). In the figure, we can see how the selection rules create states which are not coupled, for example 2 for $\sigma^+$ light, -2 for $\sigma^-$ or 0 for linearly polarized light [33]. Being the dark state invisible to light, it will not experience any energy shift and its potential will be flat. Contrarily, the bright states will experience a shift in the energy levels, due to local polarization gradient and laser intensity.
The cooling process can be explained as follows, Fig.3.4(b).
A moving atom in a dark state will be coupled to a bright state because its velocity is $v \neq 0$. This happens because the dark and bright states are not stationary when the atom velocity is different from zero, in the dressed-state picture in fact the kinetic term induces oscillations between the two states [33]. The residence time of an atom in the dark state is $\tau_D \propto 1/(vk)^2$, with wavevector $k$, and the probability of coupling has a maximum when the atom is closer to the potential minima of the bright state. When the atom is coupled via motional coupling to the bright state, it climbs the potential hill and when it reaches the peak is pumped back to dark state. This leads to cooling, in fact an energy equal to the difference between the bright and dark state is dissipated. Slow atoms are accumulated in dark states, which subsequently leads to lower and lower temperatures.

## 3.3 Optical Dipole Trap

Temperature is not the only limit encountered in a MOT, in fact important limitations exist also for the phase-space density of the atoms in the trap. To overcome this limitations and achieve a phase-space density necessary for the observation of quantum degeneracy, a conservative trap and a following evaporative cooling is necessary.
In Section 2.3 we described the interaction of light and matter, introducing the con-

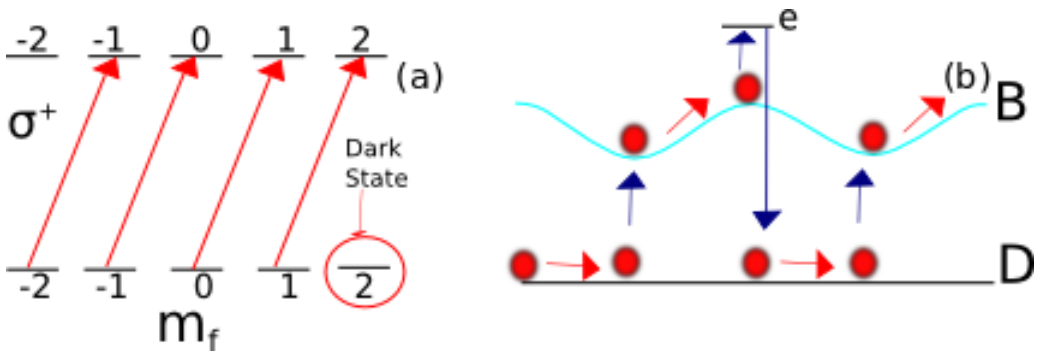



*Figure 3.4: (a)The magnetic substate $m_F = 2$ is a dark state in the particular case of the transition $F = 2 \rightarrow F' = 2$ with $\sigma^+$ light. (b) The combined effect of VSCPT and optical pumping to give rise to Gray molasses cooling. Red arrows indicate the spatial propagation of the atom while blue arrows indicate possible transitions.*

cept of dipole force. In order to create such a trap, the dipole force plays a crucial role. Equation (2.13) describes the dipole potential and consequently the dipole force is defined as $F_{\text{dip}} = -\nabla U_{\text{dip}}$. Equations (2.15) and (2.16), which describe the dipole potential $U_{\text{dip}}$ and the scattering rate $\Gamma_{\text{sc}}$ are recalled here for convenience [21]

$$U_{\text{dip}}(\mathbf{r}) = \frac{3\pi c^2}{2{\omega_0}^3}\frac{\Gamma}{\Delta}I(\mathbf{r})$$

$$\Gamma_{\text{sc}}(\mathbf{r}) = \frac{3\pi c^2}{2\hbar{\omega_0}^3}\left(\frac{\Gamma}{\Delta}\right)^2 I(\mathbf{r})$$

For a red detuned laser beam ($\Delta < 0$) $U_{dip}$ is negative and $F_{dip}$ attracts all the atoms towards the region of the beam with the maximum intensity. Furthermore, as the dipole potential scales as $I/\Delta$ and the scattering rate as $I/(\Delta)^2$, typically high intensity lasers and big detunings are used to keep the scattering rate as low as possible for a certain trap depth.

A dipole trap can be produced at the focus of a Gaussian laser beam, with the requirement of the wavelength being far from the atomic transitions. In our setup, an optical dipole trap is created by an Ytterbium laser at 1070nm with a maximum power of 100W, as explained in detail in section 4.3.

I am going to first describe in detail how a single trap works. In our system instead

we use two beams which are crossed under an angle of 13.6 degrees. The crossed trap is simply the addition of two linear traps. For Lithium, differently from what happens with other alkali elements like Caesium, we can neglect the fine and hyper-fine structure contributions, being the splitting between $2^2P_{1/2}$ and $2^2P_{3/2} \approx 1$GHz very small compared to the detuning of the dipole laser being $\approx 167$THz.

### 3.3.1 The focused beam trap

In the present section a dipole trap created by a focused beam is analyzed and explained. As mentioned previously, this is one of the methods for the creation of an optical dipole trap, as well as a crossed beam trap (used in this experiment) and the standing wave trap.

The focused beam trap is the simplest among the different methods and it can be formed by one collimated beam which is focused down and re-collimated using two lenses, Fig. 3.5.

The intensity profile of this beam is given by [34]:

$$I(r,z) = \frac{2P}{\pi w^2(z)} e^{-(2r^2/w^2(z))} \tag{3.9}$$

where $P$ is the total power, $r$ is the radial coordinate and $w(z)$ is the radius at which the intensity values fall to $1/e^2$ of their axial values, at the plane z along the beam. The beam radius $w(z)$ can be written as:

$$w(z) = w_0 \sqrt{1 + \left(\frac{z}{z_R}\right)^2} \tag{3.10}$$

being $w_0$ the beam waist and $z_R = \pi(w_0)^2/\lambda$ is the Rayleigh length. The trap depth is defined as $U_0 = U_{dip}(r = z = 0)$. If the thermal energy $k_BT$ is much smaller than the trap depth $U_0$, then the dipole potential can ba assumed to be harmonic:

$$U_{dip}(r,z) = -U_0 \left(1 - 2\frac{r^2}{{w_0}^2} - \frac{z^2}{{z_R}^2}\right) \tag{3.11}$$

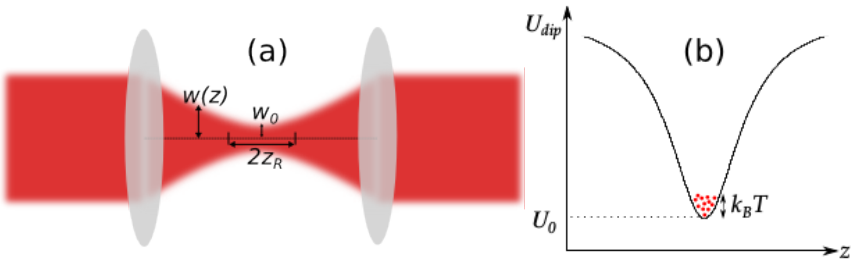



*Figure 3.5: (a)A gaussian beam travelling along $\vec{z}$ axis is focused and recollimated by a two lenses system. In the figure, $w_0$ is the beam waist and $z_R$ is the Rayleigh length. (b) The potential $U_{dip}$ vs $z$ is plotted. $U_0$ is the potential at the focus of the beam. For a red detuned dipole trap, atoms tend to accumulate in focus area of the beam*

Combining equations (2.13) and (3.9), we can express $U_0$ as:

$$U_0 = -\frac{3c^2 P}{{\omega^3}_0 {w^2}_0}\left(\frac{\Gamma}{\omega_0 - \omega}\right) \tag{3.12}$$

and the oscillation frequencies are:

$$\omega_r = \sqrt{\frac{4U_0}{m{w^2}_0}} \quad and \quad \omega_z = \sqrt{\frac{2U_0}{m{z_R}^2}} \tag{3.13}$$

In particular, the ratio between the two is $\omega_r/\omega_z = \sqrt{\frac{2\pi^2}{\lambda^2}{w^2}_0}$.

### 3.3.2 Evaporative Cooling

Evaporative cooling is a fundamental technique in ultra-cold atoms physics for the achievement of quantum degeneracy and it is normally implemented in the last stage of the cooling process. Evaporative cooling was first proposed by Harald Hess in 1986 [35] and the technique was first used in combination with laser cooling for trapped alkali atoms in 1995 [36]. This technique is based on the removal of the most energetic atoms from the trap, followed by a rethermalization of the remaining atoms by elastic collisions resulting in the reduction of the overall temperature of the system.

In order to leave the trap, an atom requires an energy greater than $U_0$, *e.g.* $U_0 + \alpha k_B T$,

with $0 \leq \alpha \leq 1$ being the energy carried away from the atom and defining the zero of energy at the bottom of the trap. the number of colliding pairs of atoms with enough energy for one to leave the trap is determined by the tail of the Boltzmann distribution. Defining the truncation parameter $\eta = U_0/k_BT$, we can write the atom loss rate [37]:

$$\dot{N} = -Nn_0\sigma\bar{v}\eta e^{-\eta} \tag{3.14}$$

where $n_0$ is the density, $\sigma$ is the atom-atom scattering cross-section and $\bar{v}$ the mean relative velocity of the atoms in the trap. We can see from this equation that the atom loss rate depends on the atom-atom scattering cross-section, which can be used to improve the evaporation by means of the Feshbach resonance.
Thus, the rate of change of the total energy of the trapped gas is:

$$\dot{E} = \dot{N}(U_0 + \alpha k_BT) \tag{3.15}$$

and the fraction of energy carried away can be calculated from the s-wave Boltzmann equation with $kT \ll U$, being $\alpha = \dfrac{\eta - 5}{\eta - 4}$ for any potential that is harmonic near the minimum.
As the evaporation progresses and the temperature drops, the evaporation rate accordingly decreases and eventually stagnates. This happens in fact, since $\eta$ increases as the temperature decreases and being $\dot{N} \propto e^{-\eta}$. In order to avoid stagnation and start evaporation again, a decrease of the trap depth is desirable. A time dependent potential can generally be written as [38]:

$$U(x,t) = -U(t)g(x) \tag{3.16}$$

where $U(t)$ contains the time dependence and $g(x)$ the spatial trap shape, with $g(0) = 1$ and $g(|x| \to \infty) \to 0$. In this case, an energy change arises from the fact that the potential energy changes. Since the atoms vibrate near the trap bot-

tom in an approximately harmonic potential, the average potential energy is (virial theorem):

$$< U >= \frac{E}{2} \tag{3.17}$$

The potential energy then changes at a rate $\left(\dot{U}/U\right) E/2$ and taking this into account in the total energy Eq.(3.15) we have :

$$\dot{E} = \dot{N}(U_0 + \alpha k_B T) + \frac{\dot{U}}{U}\frac{E}{2} \tag{3.18}$$

Solving the above equation for a fixed value of $\eta$, the number of trapped atoms is found to vary with trap depth as:

$$\frac{N}{N_i} = \left(\frac{U}{U_i}\right)^{\left(\frac{3}{2(\eta'-3)}\right)} \tag{3.19}$$

where i denotes the initial condition at $t = 0$ and $\eta' = \eta + \alpha = \eta + (\eta - 5)/(\eta - 4)$. The corresponding scaling of the PSD (Phase-Space-Density), which for a harmonic trap is $\rho = N\left(\frac{\hbar\omega}{k_b T}\right)^3$, can be deducted straightforwardly from Eq.(3.19):

$$\frac{\rho}{\rho_i} = \left(\frac{U_i}{U}\right)^{\left(\frac{3(\eta'-4)}{2(\eta'-3)}\right)} = \left(\frac{N}{N_i}\right)^{(\eta'-4)} \tag{3.20}$$

In our experiment, an initial PSD of $10^{-4}$ and a decrease of $10^3$ factor in the trap depth lead to a decrease in the atom number of a factor 10 and a PSD$\approx 1$.

These scaling laws were derived neglecting background gas collisions. In order to include them, a further scaling factor $-\Gamma_{\rm bg} E$ must be included in Eq.(3.14) and consequently in Eq.(3.18). What is found at the end of the treatment including the background collisions is that all of the previous scaling laws are furtherly reduced by a factor $e^{-\Gamma_{\rm bg} E t}$, being $t$ the time over which the trap depth is lowered.

## 3.4 Imaging

Optical diagnostic is extremely important for getting information from the atomic cloud. Exploiting the absorption of a weak light beam through the cloud we can get the density profile of the same, while observing how the cloud expands can give us important information like the temperature, obtained after appropriate software analysis.

The interaction of atoms with a beam of light involves three processes: spontaneous absorption of photons, re-emission of photons, and shifting the phase of the transmitted light. These processes are strictly related to the following techniques: absorption imaging, fluorescence imaging and dispersive-non destructive imaging. In this experiment absorption imaging is the most used technique used for probing the cloud, but in the future a non destructive imaging system will be implemented and is one of the next goals.

The interaction of the probing light and the atomic cloud sample can be described using the imaginary index of refraction $n_{\text{ref}} = n_r + in_i$. Assuming $n_{\text{ref}} - 1 \ll 1$ and in the limit of $I/I_{\text{sat}} \ll 1$, , the index of refraction of a dilute atomic vapor is directly related to the atomic density $n$ as [39]:

$$n_{\text{ref}} = 1 + \frac{\sigma_0 n \lambda}{4\pi} \left[ \frac{i}{1 + {\Delta_{\Gamma/2}}^2} - \frac{\Delta_{\Gamma/2}}{1 + {\Delta_{\Gamma/2}}^2} \right] \tag{3.21}$$

with $\sigma_0$ the on resonance cross-section, $\lambda$ the wavelength of the probe beam and $\Delta_{\Gamma/2} = \dfrac{\omega - \omega_0}{\Gamma/2}$ is the detuning of the probe beam in terms of half-linewidths. Making the "thin lens" approximation, atoms attenuate and phase shift the probe light and the electric field of the probe beam after the cloud differs from the electric field before the cloud:

$$\mathbf{E}(x, y) = \mathbf{E}_0(x, y) \exp\left( -\frac{2\pi i}{\lambda} \int \left[ n_{\text{ref}} - 1 \right] dz \right) = t\mathbf{E}_0(x, y) e^{i\phi} \tag{3.22}$$

with $t$ being the transmission coefficient and $\phi$ the phase-shift. These parameters both depend on the column density $n_z = \int n dz$ and $\sigma_0$:

$$t = e^{D/2} \tag{3.23}$$

$$\phi = -\Delta_{\Gamma/2}\frac{D}{2} \tag{3.24}$$

having introduced the off-resonance optical density $D = n_z\sigma_0/(1 + {\Delta_{\Gamma/2}}^2)$.
After passing through the atomic cloud the imaging beam is subsequently directed towards a CCD camera. The camera photosensor is not able to detect phase shifts, while it can instead detect variations of the intensity of the laser beam, strictly related to $t^2$.
The change of the Intensity $I$ in the resonant probe beam during propagation through the sample along the $\vec{z}$ direction can be described as:

$$\frac{dI}{dz} = -In_z\sigma_0 \tag{3.25}$$

Integrating (3.25) yields to:

$$I = I_0 e^{-\sigma_0 n_z} \tag{3.26}$$

Therefore, the column density $n_z$ is:

$$n_z = -\frac{1}{\sigma_0}\mathrm{Ln}\frac{I}{I_0} \tag{3.27}$$

and the atom number can be obtained integrating:

$$N = \int n_z(x, y)dxdy \tag{3.28}$$

### 3.4.1 Measuring the Temperature

A fundamental information that can be achieved through imaging techniques is the temperature of the cloud. The standard technique used for performing such a

measurement is called Time-Of-Flight (TOF) imaging. The atoms are released from the trap and they are imaged at different falling times. The expansion of the cloud is analyzed and from the increase of its size the temperature can be inferred. The fundamental assumption under this technique is the repeatibility of the experiment, thus the capability of the setup to produce the same initial conditions each time. For each shot we effectively destroy the cloud and we need to produce a new one for the next shot at a different fall time. A very stable apparatus is thus required for performing confidently this type of measurement.

When atoms are in the trap, their energy can be expressed as:

$$\epsilon(\mathbf{r},\mathbf{p}) = \sum_i \frac{m{\omega_i}^2{r_i}^2}{2} + \frac{p^2}{2m} \tag{3.29}$$

where $m$ is the mass of the atoms, $\omega_i$ is the oscillation along $\hat{x}, \hat{y}, \hat{z}$, $p$ is the momentum and $r_i$ is the position of the atoms. The probability distribution of the atoms inside the trap at a time $t = 0$ is given by, [40]:

$$f_0(\mathbf{r}_0,\mathbf{p}) = e^{\mu/k_BT} e^{-\epsilon(\mathbf{r}_0,\mathbf{p})/k_BT} \tag{3.30}$$

For a free expansion without interaction, the gas follows the classical dynamics: $dr/dt = \mathbf{p}/m$ and $d\mathbf{p}/dt = 0$. These equations describe the evolution of the system, the new position $\mathbf{r}$ at a time $t$ is given by $\mathbf{r} = \mathbf{r}_0 + \mathbf{p}t/m$. The distribution function, at the position $\mathbf{r}$ is:

$$f_t(\mathbf{r},\mathbf{p}) = f_0(\mathbf{r}\text{-}\mathbf{p}t/m,\mathbf{p}) = e^{\mu/k_BT} e^{-\epsilon(\mathbf{r}\text{-}\mathbf{p}t,\mathbf{p})/k_BT} \tag{3.31}$$

Integrating this equation over all the momenta yields to the density distribution of the gas:

$$n(\mathbf{r},t) = e^{\mu/k_BT} \frac{1}{\lambda_{dB}} \prod_i \sqrt{\frac{1}{1+{\omega_i}^2t^2}}\, e^{\frac{-m{\omega_i}^2{r_i}^2}{2k_BT(1+{\omega_i}^2t^2)}} \tag{3.32}$$

Each factor in the latter expression is a gaussian of width

$$\sigma^2 = \frac{k_B T^2 t}{m} \tag{3.33}$$

Thus, at a time $t$ the width of the distribution will be:

$$\sigma_t{}^2 = \frac{k_B T t^2}{m} + \sigma_0{}^2 \tag{3.34}$$

By measuring the sizes of the cloud as a function of time, the temperature can be calculated. Shown in Fig. 3.6(top) is a temperature measurement of the dipole trap after 1s of plain evaporation time (see section 4.3 for details). The Gaussian widths $\sigma_x(t)$ and $\sigma_y(t)$ are measured as a function of the time of flight and from a linear regression fit the coefficient $k_B T/m$ is obtained and thus the temperature $T$. Fig. 3.6(bottom) shows the expansion of the atomic cloud as a function of time. For a more accurate measurement, a longer time of flight should be chosen, but this implies a lower signal to noise ratio and a less accurate determination of the size of the cloud. As outlined before, this method gives a precise estimation of the temperature when the cloud can be treated classically. Once quantum degeneracy is achieved, the assumptions made here are no longer valid and because of the interactions a precise measurement of the temperature is more challenging. Nevertheless, for the thermal part of a condensate, whose description is still Gaussian, this technique remains valid.

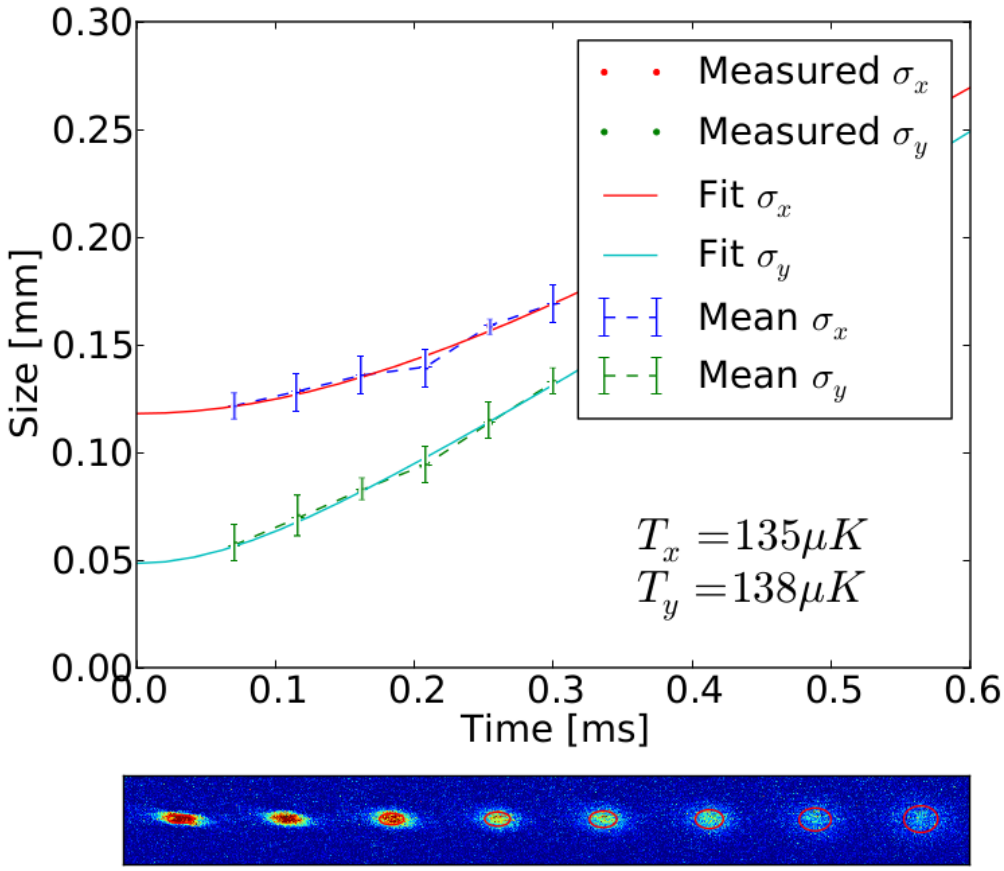



*Figure 3.6: (Top)The temperature of the dipole trap is obtained through a linear regression as explained in this section. Sizes are plotted versus TOF. Error bars are obtained through standard deviation of three equal measurements.*
*(Bottom)The sizes of the cloud for different fall times are outlined. As the cloud expands, the signal to noise ratio decreases and that makes it more challenging to identify correctly the sizes of the cloud*

# Chapter 4

# Experimental apparatus

This chapter gives a more detailed description of the experimental apparatus built for the realization of the experiment. It is my intention in this chapter to focus on those aspects where my contribution has been fundamental for the prosecution of the experiment.

## 4.1 Laser Setup

In order to put into practice the laser cooling theory explained in the previous sections, a very precise control of the frequencies and intensities of the lasers is necessary. The light that we use everyday in the experiment is produced by ECDLs, external cavity diode lasers, and the frequency shifts are controlled by a piezoelectric crystal. The piezo can be externally controlled to vary the frequency of the lasers. Light frequency and intensity can be furtherly modulated using another fundamental device, the AOMs, acusto-optic modulators. Mechanical shutters are also widely used to control which beams need to be switched on or off in the expermental sequence.

In the following sections a full description of the laser scheme is given for the production of the MOT light and the lasers used for the dipole trap beam.

*Table 4.1: My caption*

| Name | Role | Output Power |
|---|---|---|
| Reference | Used for spectroscopy to lock the frequency of the other lasers. | 15mW |
| Imaging | Used for absorption imaging at low and high field | 15mW |
| Toptica TA Pro | Provides seed light for the homebuilt TA and re-pumping light for the MOT and Zeeman slower. | 350mW |
| Homebuilt TA | Provides cooling light for the MOT and Zeeman slower. | 300mW |

### 4.1.1 Overview

The $^6$Li laser systems consists of a reference laser, the Toptica TA Pro at 670nm (TA-670), a homebuilt tapered amplifier and an imaging laser. Power values of these lasers are shown in table 4.1, while a $^6$Li level scheme with the relevant transitions is depicted in Fig. 4.1.

Recalling the notion of total atomic angular momentum $F$ introduced in the first chapter, being the nuclear momentum $I = 1$ for $^6$Li and the total angular momentum $J = 1/2$ for the ground state and $J = 3/2$ for the excited state, we have that the coupling of $J$ and $I$ leads to $F = 1/2, 3/2$ for the ground state and $F' = 1/2, 3/2, 5/2$ for the excited state.

The reference laser is locked to the crossover of the transitions from the $F = 1/2$ and $F = 3/2$ ground states to the overlapped $D_2$ excited states through Doppler-free absorption spectroscopy, as explained in detail in previous works in the same lab, [14], [41]. The TA-670 and imaging lasers frequencies can be tuned with respect to the reference lasers frequency, through offset locks, [14], [41].

An overview of the setup is given in Fig. 4.5. The TA-670 delivers 350mW of light with a seed of $\approx$ 28mW and is divided into two beams containing 325mW and 25mW of power. The 325mW beam provides the MOT repumper light while the 25mW beam is used as a seed for a home-built tapered amplifier system to

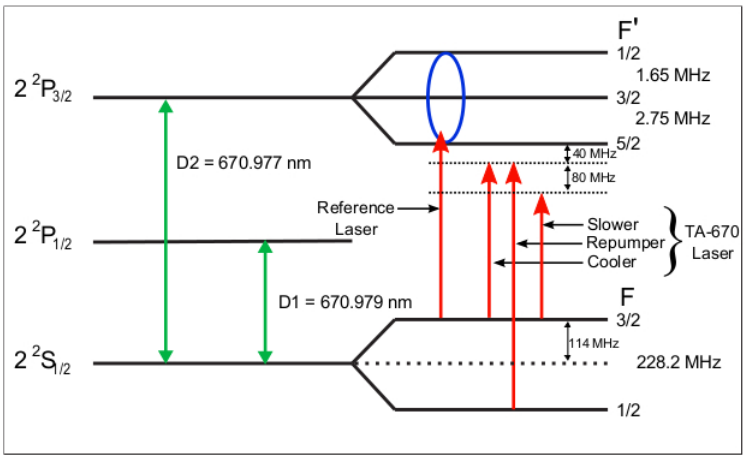



*Figure 4.1: Scheme of the $^6Li$ transitions and light beams used in the experiment*

provide enough light for the MOT cooler beams. The output power of the home-built TA, after passing through an optical isolator, is 300 mW. The MOT cooler and repumper beams are subsequently shifted using AOMs by $-114$MHz and $+114$MHz, respectively. At this point, after being shifted by the AOMs the cooler beam is red-detuned from the $F = 3/2$ to $F'$ transition and the repumper beam is red-detuned from the $F = 1/2$ to $F'$ transition. After passing through the AOMs, the two beams are then recombined using a polarising beam splitter (PBS) and with the help of other two PBSs four beams are produced: three MOT beams and one Zeeman slower beam. The Zeeman slower beam is furtherly shifted by an AOM of $-80$MHz. The imaging laser is instead shifted of $-114$MHz like the cooler beam, in order to be resonant with the same transition.

## 4.2 The Magneto Optical Trap

The creation of a Magneto Optical Trap requires a dissipative force for momentum confinement given by the light and a gradient force, given by a magnetic quadrupole field, for spatial confinement. In this experiment, the light necessary for the production of the MOT is produced by the lasers and the apparatus discussed in the

*Table 4.2: My caption*

| Laser | Detuning(MHz) | Output Power(mW) |
|---|---|---|
| MOT cooler | -40 | 20-25 |
| MOT repumper | -40 | 15-20 |
| Slower cooler | -120 | 10-15 |
| Slower repumper | -120 | 10-15 |

previous section and it is prepared on a different optical table than the one where the main chamber is located. Then, it is transferred to the vacuum chamber through polarisation maintaining optical fibres. At the output side of the fibres, outcouplers with 10 mm lenses are used for light collimation. The optical fibres used have a numerical aperture of 0.12 which results in beams with a $1/e^2$ radius of 12 mm. Three optical fibres carry the X,Y,Z MOT light and a separate one carries the light for the Zeeman Slower. Each MOT light beam is then retro-reflected to make up six beams. Because of the unresolved excited state and the impossibility of selecting a specific sub-state, a higher power in the repumper is required, compared instead to other alkali species like Caesium. Powers of the fibers used in the experiment are reported in table 4.2.

The collimated light after the outcoupler needs to be aligned in the center of the vacuum chamber for the production of the MOT in combinement with the magnetic field. This is done by placing irises in the optical fibre out-couplers and using paper templates with 1 mm pinholes on both sides of the chamber. We found that perfect retro-reflection of the MOT beams gives a more stable and reliable loading of the dipole trap, even if a slight misalignment could bring to an increase in the MOT atom number.

At this point, characterization of the MOT and improvement for a good loading of the dipole trap is carried out. Optimization is performed by changing different parameters and observe the behaviour of the cloud as they vary. The goal of this step of the experiment is to achieve a high atom number in the mot, while keeping the temperature of the cloud as low as possible. The detuning is found optimal to

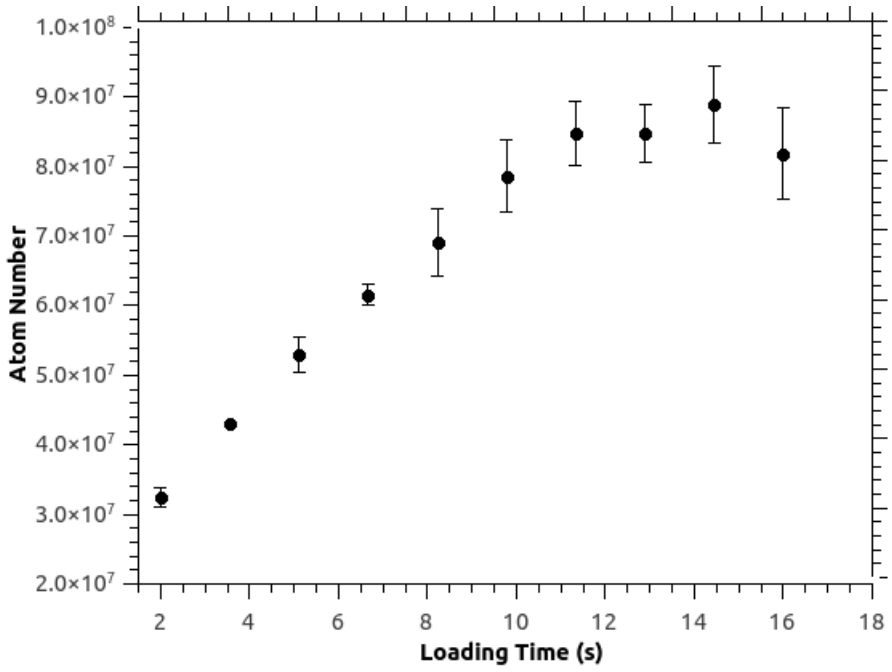



*Figure 4.2: Loading of the MOT vs time. Saturation occurs at approximately 12s. Typically a shorter time in the sequence is used for the optimum loading of the dipole trap*

be around 40MHz (6.8Γ) during the loading and it changes accordingly for the MOT light and the Slower. A typical MOT sequence lasts $\approx 5 - 10s$, Fig. 4.2.

### 4.2.1 Compression phase and transfer into Dipole Trap

The transfer of the atoms from the MOT to a dipole trap is a fundamental step for the realization of our experiment. Typically, we want a high atom number and a very low temperature in the dipole trap, together with an equal mixture of atoms in the two sub-states $|F = 1/2, m_F = 1/2\rangle$ and $|F = 1/2, m_F = -1/2\rangle$. This requirement is necessary for effective evaporative cooling, collisions are in fact suppressed for fermions in the same state, [42].

We previously described, Sec.3.2.1, the mechanism that leads to a limit in the temperature achievable in a mot, which we recall for $^6Li$ being $T_D = 141\mu$K. Obtaining this limit temperature is a consequence of considering an atom as a two-level system, while instead the complexity of the atomic structure and the unresolved excited

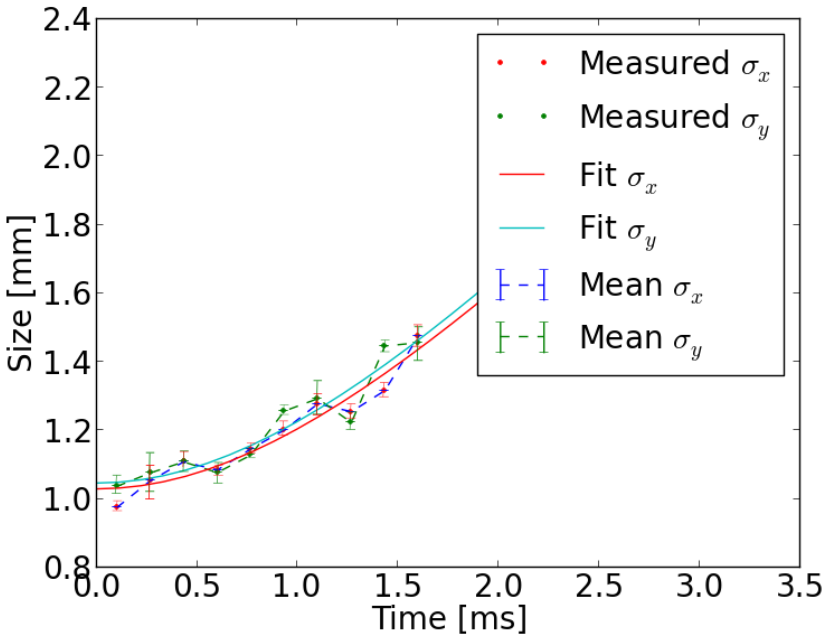



*Figure 4.3: Temperature of the MOT measured after compression stage. Temperatures obtained are : $T_x = 367\mu$K and $T_y = 381\mu$K. The mismatch between the two temperature is due to a different expansion of the cloud along the two axes.*

state would lead to a higher minimum temperature. We saw how this minimum is reached when the detuning reaches the value $-\Gamma/2$. For this reason after loading the MOT we bring the detuning closer to resonance, until the value $-\Gamma/2(2.8\text{MHz})$. This results in a compression of the cloud, that gets denser and colder. In our experiment the compression phase time is of 25ms and in this framework the MOT temperature drops from $\approx$ 1mK to $\approx 370\mu$K, Fig. 4.3.

Finally, in order to prepare the atoms for the loading of the dipole trap, we need to make sure that atoms are optically pumped in the two ground states $|F = 1/2, m_F = \pm 1/2\rangle$. This is done in order to avoid inelastic, spin changing collisions in the dipole trap, [43]. Collisions between atoms in the different $m_F$ states provide in fact rethermalisation during evaporative cooling. Producing this spin-mixture is achieved by turning off the repumper light for 1 ms before the cooling light at the end of the MOT stage.

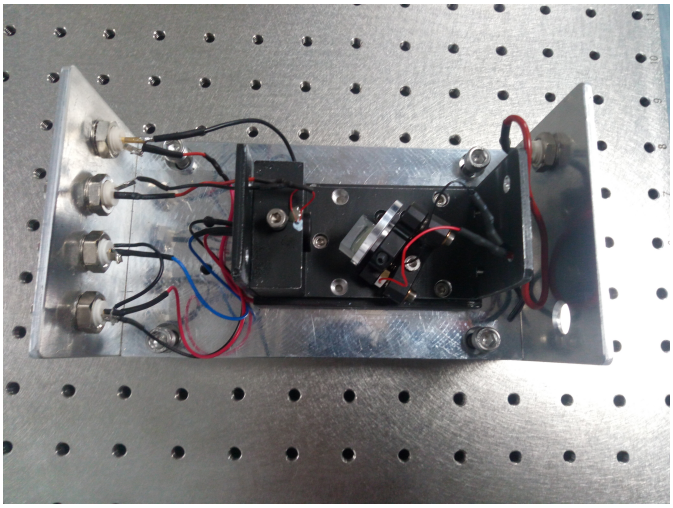


*Figure 4.4: The homebuilt ECDL operating on the $D_1$ line*

### 4.2.2 Sub-Doppler cooling of Lithium

The unresolved excited state $2^2P_{3/2}$ prevents us from reaching Sub-Doppler cooling using well established techniques commonly applied on the $D_2$ line to other species like Caesium, [44]. Sub-Doppler cooling is found to be a powerful technique to increase the phase-space density, leading to a greater efficiency of the dipole trap loading and consequent observation of quantum degeneracy. Thus, many efforts have been made in order to find alternative laser cooling scheme which can be effective for species with a narrow excited state linewidth, like Lithium or Potassium. We are currently implementing a sub-Doppler scheme, based on the Gray-molasses cooling technique on the $D_1$ line, following the example explained in [45], [29].
Many important aspects have been taken in consideration when deciding to implement this cooling method. Firstly, the price of the required components was not high, having to build only a new laser operating on the $D_1$ line. Secondly, the possibility of implementing the new cooling scheme exploiting the pre-existent setup without modifying it. Thirdly, the integration of the new apparatus does not require much physical space and can be easily adapted on the existing optical table. The description of the apparatus follows.

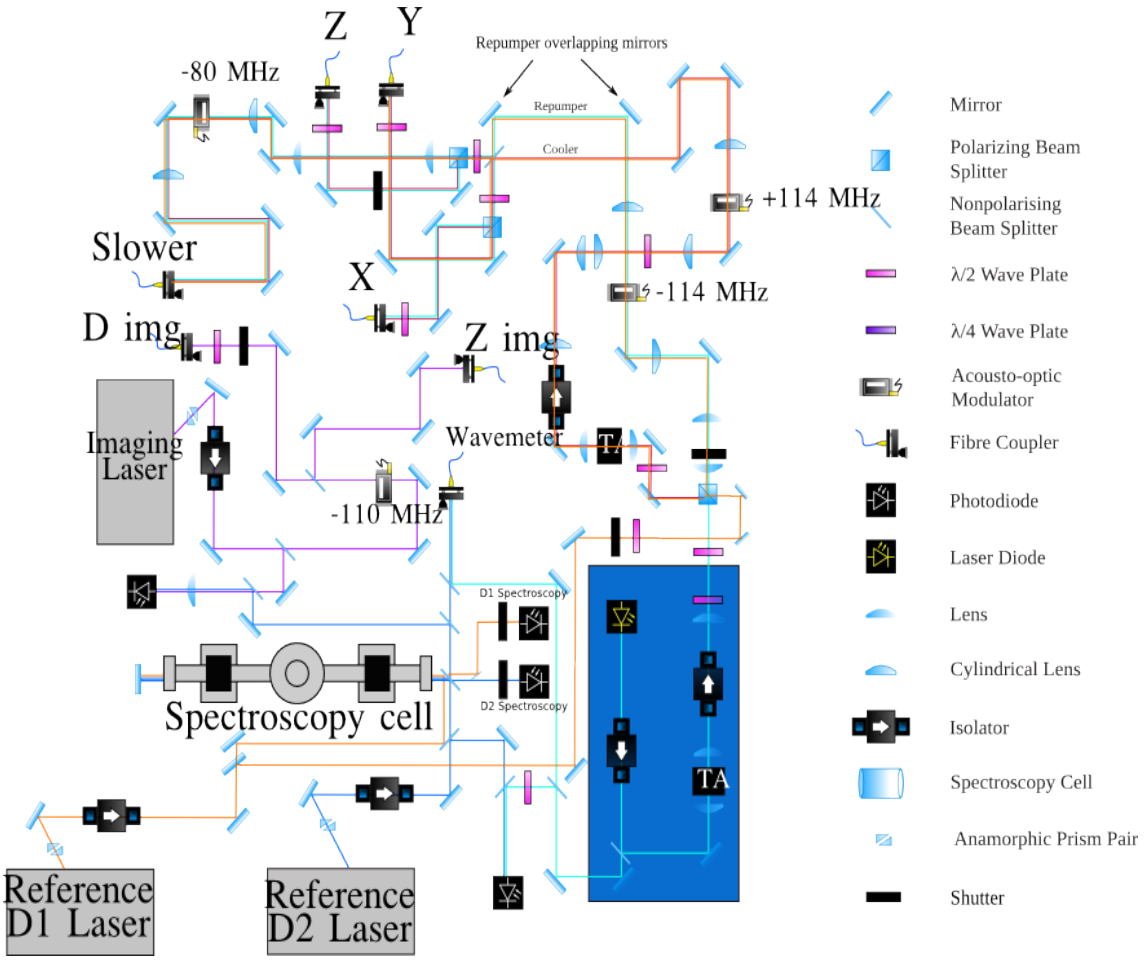



*Figure 4.5: The scheme of the Gray-molasses apparatus and the optical table*

A new laser operating on the $D_1$ line has been built. We used a HL6545MG laser diode ( 660 nm, 120mW, single-mode ) and heated to $\approx 70°C$, Fig.4.4. This diode can output 120mW and the beam is subsequently splitted by a non polarising beam splitter. The weaker beam is sent to the vapour cell in order to get the spectroscopic signal of the $D_1$ transition. Once this signal is obtained from the photodiode, it is fed into a lock-in amplifier and the laser is now locked with the right frequency. The stronger beam will instead be coupled on a PBS with the existing TOPTICA TA-PRO 670nm laser beam and will follow the path of the pre-existing repumper beams, without adding further optics. The PBS will split the beam in two further beams: one will follow the $D_2$ repumper beam and will be coupled to the MOT fibers; the other will be injected into the Homebuilt Tapered Amplifier and will provide $D_1$ cooling light, overlapped with the existing $D_2$ one. An AOM will be used as a switch to enable the $D_1$ light when necessary.
With this configuration, 2-3mW of repumper light per fiber and 10-12mW of cooler light per fiber will be available for the Sub-Doppler cooling in our setup. The $D_1$ Gray molasses light will be shone during the last stage of the MOT compression and will allow the atoms to cool down and reach temperatures as low as $\approx$ 40-50 $\mu$K.
Presently, the laser needs to be sent to the vapour cell for the $D_1$ locking; data collection and optimization of the sequence will follow.

## 4.3 Dipole Trap

After atoms have been trapped and cooled by the MOT, they are transferred into a far-off-resonance optical dipole trap for further cooling. The Dipole trap is produced by a multi-mode 100 W IPG Yb fibre laser and the beam has a wavelength of 1070 nm. The fibre laser provides a $TEM_{00}$ mode which is collimated to a diameter of 5mm. At the centre of the dipole trap, the beam is focused to a width of 90$\mu$m. The optics used in the in the realization of the dipole trap is made of fused silica which is advantageous against thermal lensing effects. Of the $\approx 10^8$ atoms in the trap after

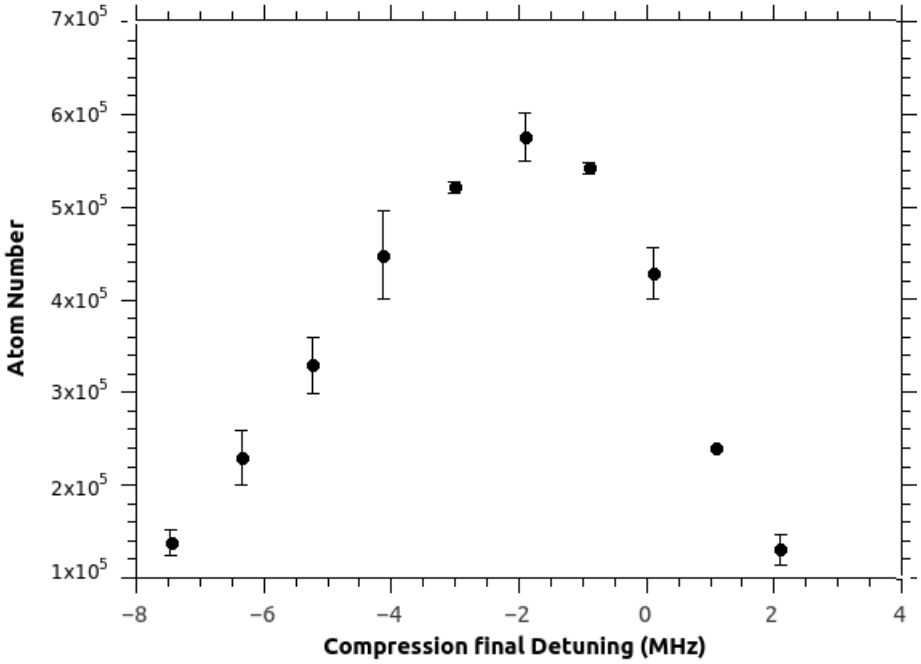



*Figure 4.6: The graph shows the maximum atom number obtained in the loading of the dipole trap. This corresponds to the detuning value where the temperature is minimum :* $-\Gamma/2$

MOT compression phase, about $10^6$ atoms are transferred in the dipole trap, in a mixture of the two lowest hyperfine ground states ($|F = 1/2, m_F = \pm 1/2\rangle$).

As it can be seen from Fig. 3.6, after loading the dipole trap and after $1s$ of plain evaporative cooling, the temperature drops from the $\approx 380\mu$K of the MOT to $\approx 140\mu$K. During this time, the trap depth is kept constant at its maximum with a magnetic field of 800G and no forced evaporation is applied. The temperature drops because of elastic collisions mechanism loss. For a non interacting gas, loss is expected predominantly from collisions with energetic background particles; this is the so called "one-body losses" mechanism. Interacting particles, on the other hand, have additional loss mechanisms such as elastic collisions in which after the collision, one of the particles results with enough kinetic energy to leave the trap. As the most energetic atoms leave the trap, the remaining atoms in the wings start accumulating in its focus.

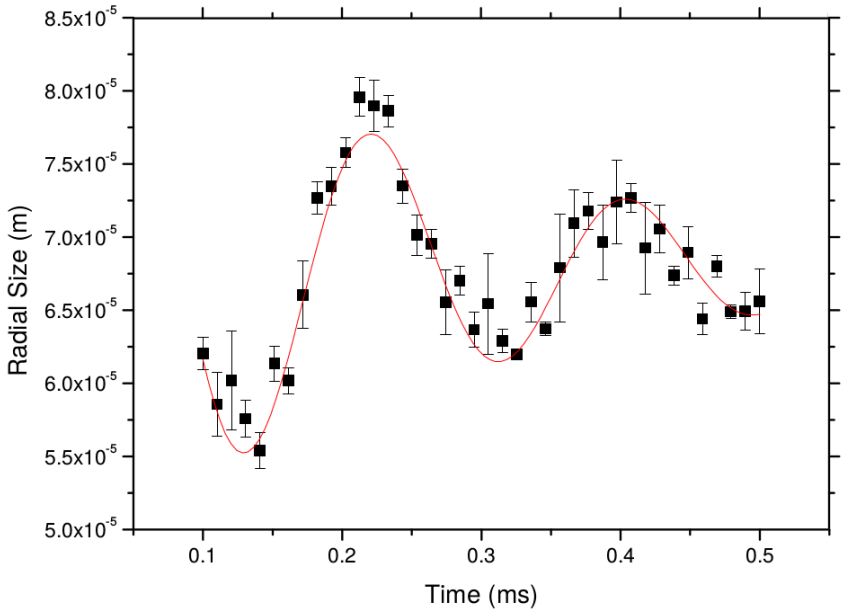


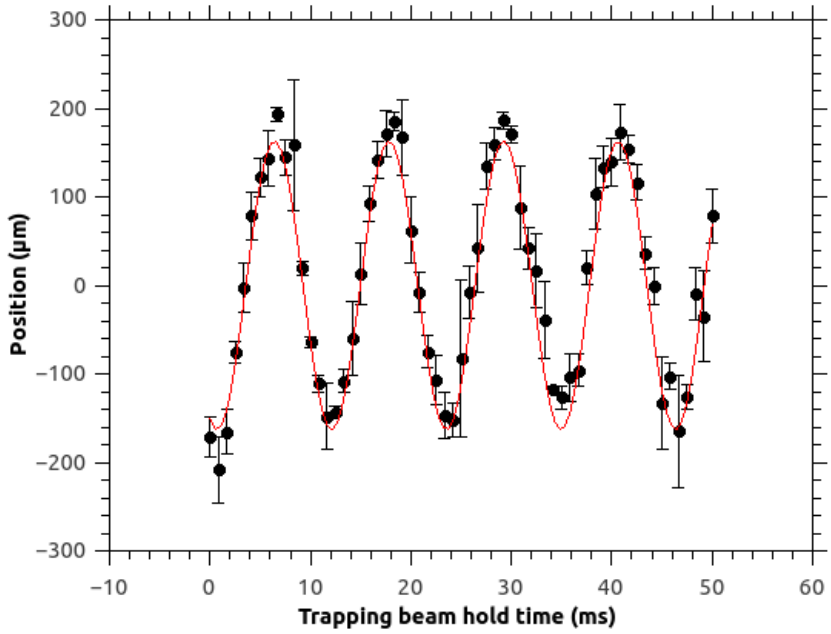

*Figure 4.7: Breathing-mode radial oscillation trap frequency measurement. The size of the atomic cloud is measured as a function of time after a sudden change in the trap frequency at $t = 0$ μs. The cloud radius is thus determined by fitting a Gaussian to the profile of the cloud and the standard deviation of the Gaussian is used as the radius. This measurement was carried out at 24 W of dipole laser power, by A.Mandoki, [14].*

### 4.3.1 Trapping frequencies

For the In situ characterization of the condensate, a full knowledge of the characteristics of the harmonic trap occupied by the atoms is necessary. At high laser powers, the trap frequency $f$ is related to the power $P$ according to this law : $f = A\sqrt{P}$, being $A$ a proportionality constant, measured for the radial and longitudinal frequencies. The values of $A$ are $525\text{HzW}^{-1/2}$ for the radial freq. and $62.7\text{HzW}^{-1/2}$ for the longitudinal.

For this experiment, the frequencies for the trap created with the IPG laser have been measured using two different methods. These frequencies have been previously measured by A.Mandoki( [14]), so we repeated some measurements to confirm the accordance with the previous values.

The first method consists in measuring the trap frequencies inducing breathing-mode




2.png

*Figure 4.8: Center of Mass radial oscillation trap frequency measurement. The position of the atomic cloud is measured as a function of the "kick" legth. This measurement was carried out at 2 W of dipole laser power.*

oscillations. Experimentally this is realised by suddenly changing the trapping frequency, increasing the power of the dipole beam. Subsequently, the frequency is obtained analyzing the expansion and the contraction of the cloud as a function of time, which oscillates at twice the trap frequency, Fig.4.7.

Another method used to measure the trap frequencies consists in measuring the oscillation of the center of mass of the cloud. Applying in this case a linear bias to the trapping potential, for example a magnetic field gradient, it is possible to create a shift in the trap centre, which depends on the ratio between the trapping light power and the magnitude of the bias. If we suddenly increase the power of the trapping beam (e.g. via an AOM), the cloud will be centered at the position of the previous trap centre, while the centre of the trapping potential is now displaced. The cloud will undergo centre of mass oscillations around the new trap centre, with a frequency dependent on the new laser power settings. The advantage of this procedure is that the COM oscillation is less damped than the breathing oscillation,

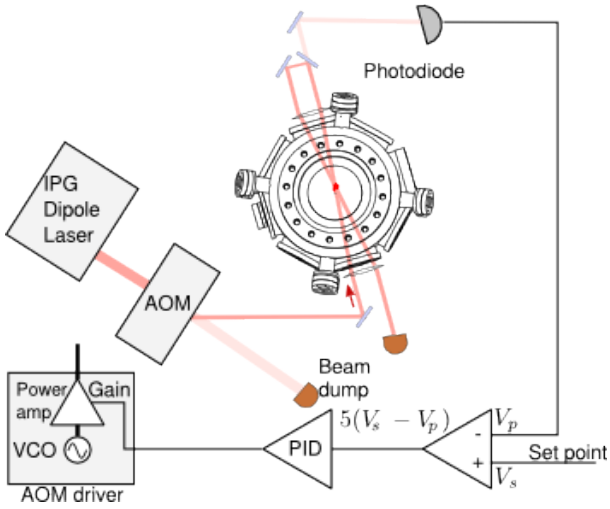



*Figure 4.9: The scheme of the feedback system used in our apparatus*

because collisional effect is reduced in this case. On the other hand, any unwanted nonlinearities in the linear bias applied may create trapping or anti-trapping forces which might affect the final measurement, Fig.4.8.

### 4.3.2 Power stabilisation

When performing evaporative cooling, a very precise control of the trap depth is required and this is the reason why a feedback loop circuit is inserted in the system. This allows us to effectively control the laser intensity, consequently we control the trap depth and we decrease the intensity fluctuations, which may cause heating and atoms loss. The feedback scheme is illustrated in Fig. 4.9 and a brief description follows. The output of the laser goes through an AOM and the first order is used to create the dipole trap. Exploiting the fact that a mirror is never 100% reflective, some dipole light is collected behind the first mirror after the chamber and is sent to a photodiode. The measured power by the photodiode is then compared with a set-point value provided by the experimental control system using a differential amplifier. The amplified signal is used as an error and goes to a PID card. The output of the PID controller is connected to the AOM driver and adjusts the power

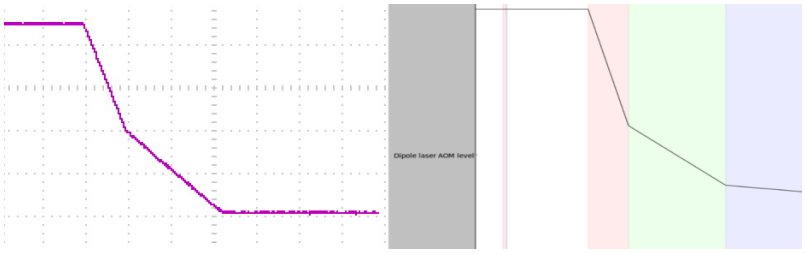



*Figure 4.10: Comparison between the evaporation ramp as seen on the oscilloscope and the evaporation ramp set on the control system*

of the RF signal going to the AOM, adjusting the amount of the beam intensity. With the help of the feedback system, evaporation ramps can be created on the control system and reproduced in a very accurate way, with some limitations. The main limitation comes from the fact that if the photodiode is set to cover the whole range of laser power, the sensitivity at the final stage of evaporation would not be the desired one. This is a critical phase of the evaporation, because at very low levels the evaporation leads to quantum degeneracy and it is where we want to avoid intensity fluctuations and instability which may cause heating. A solution to this problem would be a double-feedback system, with a photodiode controllingthe highest evaporation levels and then switching to another photodiode to accurately manage low evaporation levels.

## 4.4 Evaporative Cooling

After the plain evaporation stage, further cooling is necessary to achieve quantum degeneracy. Increasing the plain evaporation time does not always lead to a temperature decrease, whereas the atom number constantly reduces because of losses mechanisms. In order to lower down the temperature of the atomic cloud, the trap depth can be reduced by lowering down the power of the dipole trap beam.
The intensity of the dipole beam can be controlled in two ways: either by changing the current applied to the IPG laser or by adjusting the diffracted light by the acusto-optic-modulator (AOM). During the evaporation stage, both ways are used.

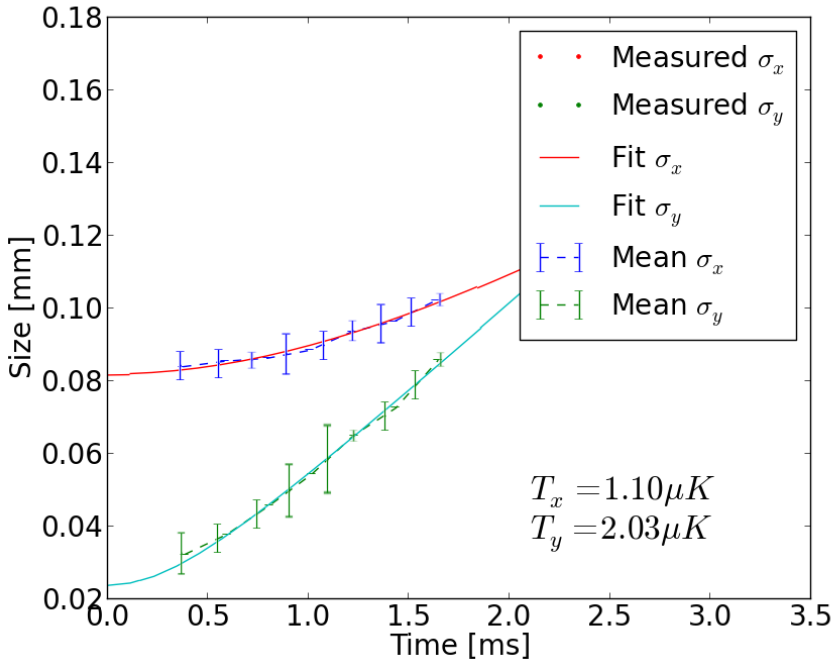



*Figure 4.11: Temperature measurement of the cloud at a trap depth of* $18\mu$K

Firstly, after 1000ms of plain evaporation, the power of the dipole beam is decreased from 100W to 30W in 500ms by lowering down the laser current. Secondly, the AOM value is decreased accordingly and two further ramps follow, with a length of 2s and 2.5s, reaching about 70mw of power.

# Chapter 5

# $^6Li_2$ BEC and In situ characterization

After the creation of a molecular gas of Lithium, evaporation is taken further as explained previously. This process will lead the molecules to a phase transition in which a macroscopic occupation of the ground state occurs. The cloud is now composed of two distinguishable parts. The molecules occupying the ground state of the potential form a condensed part, while the others form a thermal part. The physical properties of a Bose-Einstein condensate can be described accounting on the interaction between these two parts, as discussed in the following sections.

## 5.1 $^6Li_2$ molecular BEC

For a finite temperature $T_C > T > 0$, not all the molecules are in a condensed state and the global wavefunction will be $\psi = \psi_0 + \sum_{i>0} \psi_i$, where the condensed mode is $\psi_0$ and all the $\psi_i$ describe the excited modes.

The interactions between condensed and thermal part play a key role in the accuracy of the description of this system. Typically, a BEC is described using an ideal or a semi ideal approximation. For a weakly interacting gas this is a valid description because interactions dont play a fundamental role in the dynamics of the condensate.

In our system instead, a BEC is formed close to a Feshbach resonance and is thus a strongly interacting system. In this situation, an appropriate model describing strong interactions has to be used.

For a weakly interacting gas, we can use the Gross-Pitaevskii Equation(GPE):

$$i\hbar\frac{\partial\psi}{\partial t} = \left[-\frac{\hbar^2}{2m}\nabla^2 + \frac{m}{2}(\omega_x^2x^2 + \omega_y^2y^2 + \omega_z^2z^2) + g|\psi|^2\right]\psi \tag{5.1}$$

with $\psi$ being a time varying, 3D mean field wavefunction in a harmonic trap.

The effect of the inter-atomic collisions is included in the third term of the equation through the interaction coefficient $g = \frac{4\pi a_S\hbar^2}{m}$, $a_\mathrm{S}$ being the s-wave scattering length.

In our case, the scattering length to be used is $0.6a_S$, $a_S$ being the atomic scattering length, because of the interactions between molecules, as we saw in Section 2.4.1.

The GPE can be generalized including any kind of potential U which is not necessarily harmonic and more experimentally realistic potential forms may be used. The Non Linear Schrödinger Equations for our system are:

$$\left[\frac{-\hbar^2}{2m}\nabla^2 + U + gn_0 + 2gn_\mathrm{th}\right]\psi_0 = \mu\psi_0 \tag{5.2}$$

and

$$\left[\frac{-\hbar^2}{2m}\nabla^2 + U + 2gn_0 + 2gn_\mathrm{th}\right]\psi_i = \epsilon_i\psi_i \tag{5.3}$$

where U is the trapping potential, $n_0$ and $n_\mathrm{th}$ are the densities of the condensed and thermal part, $\mu$ is the chemical potential, $\epsilon_\mathrm{i}$ is the energy of the $i^\mathrm{th}$ excited level.

Equations (5.2) and (5.3) are the "Hartree-Fock" (HF) equations as they contain only two interactions, the ones shown in Fig. 5.1. In the ($a$) diagram an excited particle (wavy line) collides with a condensate atom (straight line) via the s-wave scattering interaction. In this interaction, known as the 'Hartree' interaction, the particles are left unchanged after the collision. The ($b$) diagram shows the 'Fock' interaction, where the same particles are exchanged after the collision. Similarly,

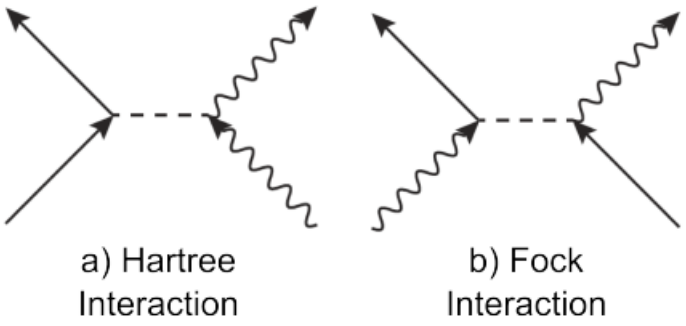



*Figure 5.1: (a) Hartree interaction. The collision between a condensate particle (straight line) and a thermal (wavy line) leaves the particle unchanged. (b) Fock interaction. The two particles are exchanged after the collision*

both excited particles may collide and and be described by the same interactions. Using the HF equations and the Bose-Einstein distribution, it will be possible to find the condensate and the thermal densities.

### 5.1.1 Ideal gas

We start our description from the non interacting case. For an ideal, non interacting Bose gas the wavefunction of the condensate solves the usual Schrödinger equation

$$\left(-\frac{\hbar^2}{2m}\nabla^2 + U(\mathbf{r})\right)\psi_0(\mathbf{r}) = \mu\psi_0(\mathbf{r}) \tag{5.4}$$

where the chemical potential $\mu$ appears because we keep the number of particles constant. For a harmonic potential, this is solved by the Gaussian wavefunction [46]

$$\psi_0(\mathbf{r}) = \frac{\sqrt{N_0}}{\pi^{3/4}a_{\rm ho}^{3/2}} e^{-\frac{1}{2}\left(\frac{x^2}{a_{{\rm ho}x}^2}+\frac{y^2}{a_{{\rm ho}y}^2}+\frac{z^2}{a_{{\rm ho}z}^2}\right)} \tag{5.5}$$

where $N_0$ is the number of particles, $a_{hok} = \sqrt{\hbar/m\omega_k}$ is the oscillator length along the $k$ axis and $a_{\rm ho}$ is the geometric mean of the ocillator lengths $(a_{{\rm ho}x}a_{{\rm ho}y}a_{{\rm ho}z})^{1/3}$.

We can extract directly the ideal condensate density distribution:

$$n_0(\mathbf{r}) = |\psi_0(\mathbf{r})|^2 = \frac{N_0}{\pi^{3/2} a_{\mathrm{ho}}^3} e^{-\left(\frac{x^2}{a_{\mathrm{ho}x}^2} + \frac{y^2}{a_{\mathrm{ho}y}^2} + \frac{z^2}{a_{\mathrm{ho}z}^2}\right)} \tag{5.6}$$

The thermal density distribution can be derived using the Maxwell-Boltzmann distribution and is given by:

$$n_{\mathrm{th}}(\mathbf{r}) = \left(\frac{m k_B T}{2\pi\hbar^2}\right)^{3/2} e^{\frac{\mu - m/2(\omega_x^2 x^2 + \omega_y^2 y^2 + \omega_z^2 z^2)}{k_B T}} \tag{5.7}$$

The density ratio between the two densities can be evaluated at the trap centre:

$$\frac{n_{\mathrm{th}}}{n_0} = \zeta\left(\frac{3}{2}\right)\left(\frac{k_B T}{\hbar\omega_{\mathrm{ho}}}\right)^{3/2} \tag{5.8}$$

so the contrast is high and a sharp peak in the spatial distribution is produced by the presence of a Bose-Einstein condensation.

This model, as simple as it is, is anyway far from an appropriate description of the dynamics involved in our system. Interactions play a key role in the formation of a condensate, so we need to include them.

As previously mentioned, we could use Eq.(5.1) to include interactions in our problem. A first simplification can be made considering the fact that for the condensate, under normal experimental conditions, the interaction term dominates on the kinetic energy, which can be neglected. This simplification does not affect the thermal fraction, in which the kinetic term is still dominant. This is the Thomas-Fermi approximation and is valid if the parameter $\frac{a_{\mathrm{S}} N_0}{a_{\mathrm{ho}}} \gg 1$, where $a_{\mathrm{S}}$ is the molecule-molecule scattering length. In normal experimental conditions this is true, because typical values for $a_{\mathrm{S}}/a_{\mathrm{ho}} \approx 10^{-3}$, so for a sample containing an atom number $N_0 \sim 10^5$ the Thomas-Fermi parameter is large enough for the approximation to be valid. Solving

Eq.(5.1) under this approximation leads to a density $n_{\mathrm{TF}}(\mathbf{r})$:

$$n_{\mathrm{TF}}(\mathbf{r}) = \frac{1}{g}\left(\mu_{\mathrm{TF}} - V(\mathbf{r})\right) \tag{5.9}$$

The chemical potential is determined by a normalization constant:

$$\mu_{\mathrm{TF}} = \frac{\hbar\omega_{\mathrm{ho}}}{2}\left(\frac{15N_0a}{a_{\mathrm{ho}}}\right)^{2/5} \tag{5.10}$$

For the case of a harmonic potential, the density exhibits the form of an inverted parabola:

$$n_{\mathrm{TF}}(\mathbf{r}) = n_{\mathrm{TF}}(0)max\left(1 - \frac{x^2}{R_x^2} - \frac{y^2}{R_y^2} - \frac{z^2}{R_z^2}, 0\right) \tag{5.11}$$

with

$$R_k = a_{\mathrm{ho}}\left(\frac{15N_0a}{a_{\mathrm{ho}}}\right)^{1/5}\frac{\omega_{\mathrm{ho}}}{\omega_k} \tag{5.12}$$

for $k = x, y, z$. In the case of isotropic trapping:

$$R = a_{\mathrm{ho}}\left(\frac{15N_0a}{a_{\mathrm{ho}}}\right)^{1/5} \tag{5.13}$$

showing how significantly the condensate spreads out in respect of the non interacting case. Another important characteristic to note is that $R$ depends now on $N_0$, while this was not true for the ideal gas.

Figure 5.2 shows the line density profile, obtained integrating over the $x$ axis. The figure shows three different stages of the evaporation, at different trap depths and after 15ms of time of flight. The profiles are fitted using the Thomas-Fermi distribution:

$$n(x) = n_{\mathrm{th}}(x) + n_{\mathrm{TF}}(x) \tag{5.14}$$

Exploiting the different expansion dynamics of the condensate part and the thermal part, a time of flight measurement is typically used when studying this system [47]. The method developed in the next sections is based on in situ measurements, *i.e.*

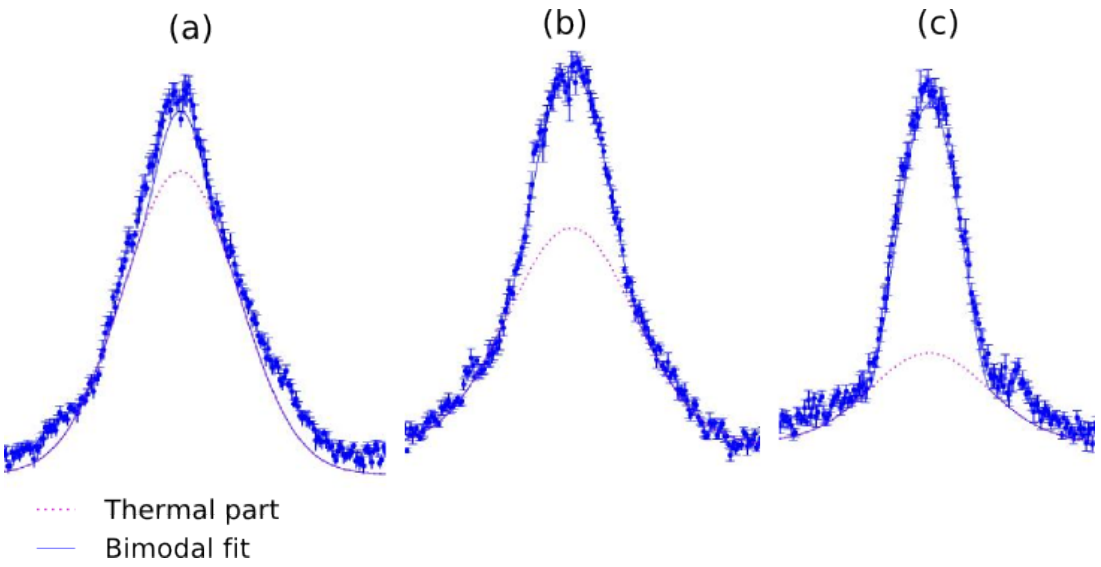



*Figure 5.2: The figure shows the system at various evaporation stages. The density is fitted using the bimodal distribution, particularly evident in the last stage.(a)The presence of a condensate is barely distinguishable. Atom number* $\approx 9 \times 10^4$*, Condensate fraction* $\approx$ 5%*, Trap depth* $2.9\mu K$*.(b)Atom number* $\approx 7.5 \times 10^4$*, Condensate fraction* $\approx$ 40%*, Trap depth* $1.8\mu K$*.(c)The presence of the bimodal distribution is evident. Atom number* $\approx 4.5 \times 10^4$*, Condensate fraction* $\approx$ 80%*, Trap depth* $1.3\mu K$*. This measurement was carried out after 15ms of time of flight. The error is the standard deviation obtained after 10 identical measurements.*

without time of flight, imaging the cloud while still in the trap. This method is meant to be more reliable for our system because of the presence of high magnetic fields that influence the dynamics of the cloud when performing time of flight measurements.

### 5.1.2 Semi-Ideal approximation

To overcome the inaccuracies of the ideal gas description, we need to include more terms in the HF equations and we need to use the full form of the Bose-Einstein distribution. In this section and in the next one, I am going to follow the derivation found in [48].

Computing the Hartree-Fock equations is not straightforward as they must be solved entirely self-consistently, therefore some approximations have to be made. The first approximation is ignoring the $n_{\text{th}}$ terms, assuming that the density of the thermal cloud is sufficiently low. The condensate will be described by the Thomas-Fermi

approximation method, as discussed in the previous section. The Bose-Einstein distribution will describe the thermal cloud and the repulsion from the condensate will be included in the total potential experienced by the thermal cloud.
In this approximation, we are thus taking into account all the collisions with the condensate, but still we are treating the thermal gas as an ideal gas. Proceeding like before, the thermal line density $n_{\rm th}(x)$ can be derived by substituting:

$$\epsilon(k,x,y,z) = \frac{\hbar^2 k^2}{2m} + \frac{m}{2}\left(\omega_x^2 x^2 + \omega_y^2 y^2 + \omega_z^2 z^2\right) + 2g n_{\rm TF}(x,y,z) \tag{5.15}$$

in the Bose-Einstein distribution, integrating over all momentum and extraneous spatial dimensions. For this integration, a continuum approach for the energy levels $\epsilon_i$ is assumed. The result is discontinuous, given the discontinuous nature of the condensate density:

$$n_{\rm th}(x) = \sqrt{\frac{m}{2\pi}}\frac{(k_B T)^{5/2}}{\hbar^3 \omega_y \omega_z} \begin{cases} \sum_{l=1}^{\infty} 2 - e^{\frac{l}{k_B T}\left(\frac{m\omega_x^2}{2} x^2 - \mu\right)} l^{-5/2} & |x| < x_{\rm TF} \\ \sum_{l=1}^{\infty} e^{\frac{l}{k_B T}\left(\mu - \frac{m\omega_x^2}{2} x^2\right)} l^{-5/2} & |x| > x_{\rm TF} \end{cases} \tag{5.16}$$

We can see that in the limit of $k_B T \gg \mu$, the summations converge to the Gaussian distribution described in the simpler model (using the $l = 1$ term). When this condition is not satisfied, this result leads to large deviations from the relation used in the bi-modal fitting model.

### 5.1.3 Hartree-Fock method

In the semi-ideal model, we discarted the thermal density $n_{\rm th}$ from the Hartree-Fock equations. While this approximation made our problem simpler and accurate in the case of low temperatures, where effectively $n_{\rm th}$ is very low, large inaccuracies are expected to arise for temperatures close to the critical temperature $T_C$, where $n_{\rm th} \gtrsim n_{\rm TF}$. Thus, in order to accurately describe our system, the repulsion caused

by the thermal cloud has to be added:

$$n_{\mathrm{TF}}(x,y,z) = max\left\{\frac{1}{g}\left[\mu - \frac{m}{2}(\omega_x^2x^2 + \omega_y^2y^2 + \omega_z^2z^2) - 2gn_{\mathrm{th}}(x,y,z)\right], 0\right\} \quad (5.17)$$

$$n_{\mathrm{th}}(x,y,z) = \left(\frac{mk_BT}{2\pi\hbar^2}\right)^{3/2}\sum_{l=1}^{\infty}\frac{Z_{full}^l}{l^{3/2}} \quad (5.18)$$

where:

$$Z_{full}^l = exp\Big[-\frac{m}{2}(\omega_x^2x^2 + \omega_y^2y^2 + \omega_z^2z^2) + 2gn_{\mathrm{TF}}(x,y,z) + 2gn_{\mathrm{th}}(x,y,z) - \mu\Big]/k_BT \quad (5.19)$$

The solutions to these equations can be calculated iteratively and then the line density can be retrieved via integration over the extraneous variables, as it is normally done for the previous methods. The inclusion of the repulsive effects though requires larger computational resources to ensure the summations converge. Another solution is thus adopted. In this solution, the iteration is solved just once and subsequently interpolated to retrieve the fully interacting densities. The details of this method are found in [48].

### 5.1.4 Experimental comparison

The comparison between the previous two methods is done by taking absorption images while the system is still in the trap. An integration over the radial component is realized and a line density is obtained. A Matlab code is used to analyze the data and the result of the fitting gives us the values for the temperature and the condensate fraction, Figure 5.3.

As appears from the figure, predictions for the temperature and the condensate fraction for the two models are different, especially at high temperatures, where the inclusion of the term $n_{\mathrm{th}}$ plays an important role. The presence of the thermal cloud

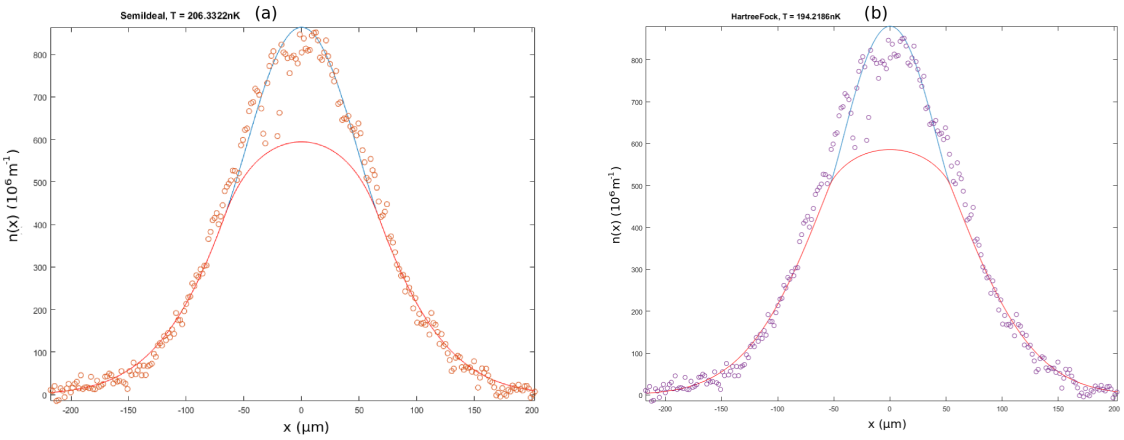



*Figure 5.3: Comparison of the fitting between the Semi-Ideal approximation (a) and the Hartree-Fock method (b). (a) T=206.3nK, Condensate fraction 15%. (b) T=194.2nK, Condensate fraction 14.2%. In both figures, the dots represent the data, the blue curve shows the fitted profile obtained with the Semi-ideal (a) and Hartree-Fock (b) models. The red curve shows the fitted thermal portion. The value of the dimensionless parameter* $1/k_F a_S$ *is 1.92*

depletes the condensate fraction because of mutual interactions and this results in a smaller condensate width, as correctly predicted by the model. This effect becomes less sizeable and visible as the temperature decreases and the two models appear to agree well. Figure 5.4 shows the condensate fraction vs temperature for a fixed interaction strength, $a = 1800a_0$ in this case. The value of the dimensionless parameter $1/k_F a_S$ is 1.92[1].

[1] $k_F$ is the modulus of the Fermi wavevector of a non-interacting gas of N trapped fermions. The Fermi energy is $E_F = \hbar^2 {k_F}^2/2m = \hbar\bar{\omega}\,(6N)^{1/3}$. Here $\bar{\omega} = (\omega_x\omega_y\omega_z)^{1/3}$ and $m$ is the mass of a single $^6$Li atom. [49]

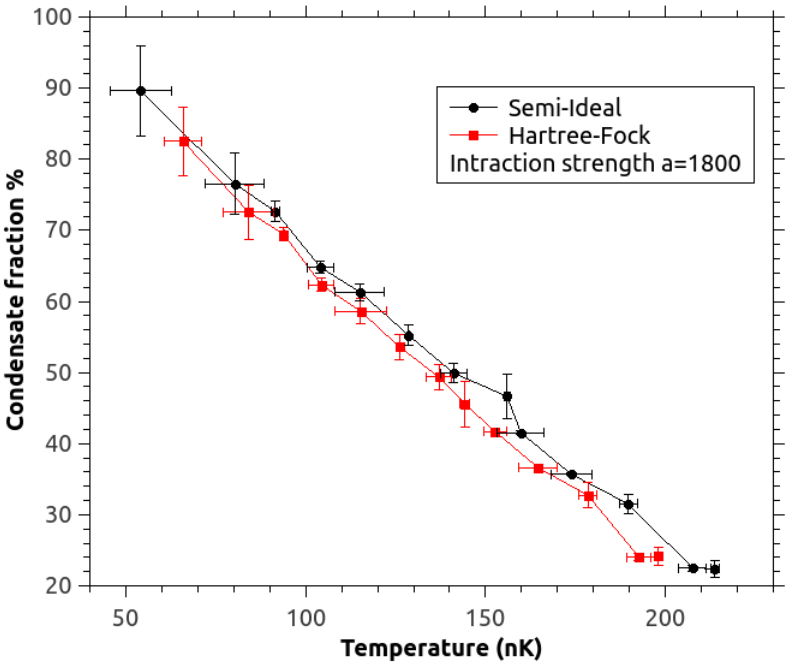



*Figure 5.4: Condensate fraction vs Temperature for a fixed interaction strength, $a = 1800a_0$. From the graph, the difference of the two description is visible particularly at high temperatures, while at low temperatures and high condensate fraction it becomes less visible. The points come from the same experimental data and the apparent difference in condensate fraction and temperature results from fitting the same data using different theoretical models*

# Chapter 6

# Conclusions

A molecular BEC is now routinely produced in the Mixture Lab of the University of Nottingham. The system is stable and capable of producing a pure condensate containing $2\times10^4$ lithium molecules. The In-Situ characterization of the condensate will be furtherly developed in the close future. New measurement at different interaction strengths will have to be performed and the demonstration that the Hartree-Fock method gives a better fit to the experimental data will follow. This is expectable because of the effects included in this method, but this statement needs statistical demonstration.

Even if the work done in this thesis has been carried out exclusively with $^6$Li, the experiment is studied and realized as a mixture experiment. The experimental sequence starts with the loading of the MOT with atoms slowed down by a dual species Zeeman slower. The atomic source is an oven that heats up a chunk of lithium to a temperature of 700K. This oven will be shortly substituted by a new dual species oven, where caesium will be added. The oven has been already completed and working and its details will be available soon in a publication. In order to overcome limitations in temperature and phase space density of the MOT, the sequence continues with the loading of the atoms in the optical dipole trap. Evaporative cooling is thus performed and a molecular state is formed, using Feshbach resonances. At this point, quantum degeneracy regime is reached and the condensate was analyzed

using different models.

A short goal is the implementation of the $D_1$ Gray molasses cooling scheme, which is expected in a near future. This cooling scheme will improve considerably the loading of atoms into the dipole trap [29] and as a consequence the evaporation stage will be much more efficient.

A new imaging method based on Faraday effect has been studied and needs to be realized. This is a non-destructive imaging method and with this technique spatially resolved images of the same cloud can be acquired many times, up to 2000 [50].

Furthermore, a double well potential apparatus is in preparation and will be implemented in the system soon. With this setup, it will be possible to observe Josephson oscillation in the double well and study the BEC-BCS crossover by controlling the interaction strength [51] [52]. As the system is designed for a double species experiment, we could use caesium as an impurity and look at the tunnelling in presence of these impurities [53] [54].

# Bibliography


[1] S. Chu, L. Hollberg, J. E. Bjorkholm, A. Cable, and A. Ashkin, "Three-dimensional viscous confinement and cooling of atoms by resonance radiation pressure," *Phys. Rev. Lett.*, vol. 55, p. 48, 1985.

[2] P. D. Lett, R. N. Watts, C. I. Westbrook, W. D. Phillips, P. L. Gould, and H. J. Metcalf, "Observation of atoms laser cooled below the doppler limit," *Phys. Rev. Lett.*, vol. 61, p. 169, 1988.

[3] E. L. Raab, M. Prentiss, A. Cable, S. Chu, and D. E. Pritchard, "Trapping of neutral sodium atoms with radiation pressure," *Phys. Rev. Lett.*, vol. 59, p. 2631, 1987.

[4] F. R.P., "Simulating physics with computers," *International Journal of Theoretical Physics*, vol. 21, pp. 467–488, 1982.

[5] I. S. et al, "Observation of feshbach resonances in a bose-einstein con- densate," *Nature*, vol. 392(6672), p. 151154, 1998.

[6] P. D.S., H. M., and S. G.V., "Observation of feshbach resonances in a bose-einstein con- densate," *Phys. Rev. Lett.*, vol. 84(12), p. 25512555, 2000.

[7] S. J. et al., "Quantum simulation of frustrated classical magnetism in triangular optical lattices," *Science*, vol. 333(6045), 2011.

[8] M. H. Anderson, J. R. Ensher, M. R. Matthews, C. E. Wieman, and E. A. Cornell, "Observation of bose-einstein condensation in a dilute atomic vapor," *Science*, vol. 269(5221), pp. 198–201, 1995.

[9] K. B. Davis, M. Mewes, M. R. Andrews, N. J. van Druten, D. S. Durfee, D. M. Kurn, and W. Ketterle, "Bose-einstein condensation in a gas of sodium atoms," *Phys. Rev. Lett.*, vol. 75, p. 3969, 1995.

[10] C. C. Bradley, C. A. Sackett, J. J. Tollett, and R. G. Hulet, "Evidence of bose-einstein condensation in an atomic gas with attractive interactions," *Phys. Rev. Lett.*, vol. 75, p. 1687, 1995.

[11] M. Zwierlein, C. A. Stan, C. H. Schunck, S. M. F. Raupach, S. Gupta, Z. Hadzibabic, and W. Ketterle, "Observation of bose-einstein condensation of molecules," *Phys. Rev. Lett.*, vol. 91, p. 250401, 2003.

[12] C. Chin, R. Grimm, P. Julienne, and E. Tiesinga, "Feshbach resonances in ultracold gases," *Rev. Mod. Phys.*, vol. 82, p. 1225, 2010.

[13] J. Nute, *A Quantum Integrated Light and Matter Interface*. PhD thesis, Department of Physics, University of Nottingham, 2016.

[14] A. Paris-Mandoki, *A Single Apparatus for the Production of Ultracold Fermionic Lithium and Cold Bosonic Caesium Gases*. PhD thesis, University of Nottingham, 2015.

[15] F. P. D. Santos, J. Leonard, J. Wang, C. J. Barrelet, F. Perales, E. Rasei, C. S. Unnikrishnan, M. Leduc, , and C. Cohen-Tannoudji, "Bose-einstein condensation of metastable helium," *Phys. Rev. Lett.*, vol. 86, p. 3459, 2001.

[16] Y. Takasu, K. Maki, K. Komori, T. Takano, K. Honda, M. Kumakura, T. Yabuzaki, , and Y. Takahashi, "Spin-singlet bose-einstein condensation of two-electron atoms," *Phys. Rev. Lett.*, vol. 91, p. 040404, 2003.

[17] A. Greismaier, J. Werener, S. Hensler, J. Stuhler, and T. Pfau, "Bose einstein condensation of chromium," *Phys. Rev. Lett.*, vol. 94, p. 160401, 2005.

[18] C. Foot, *Atomic Physics*. Oxford University Press, 2005.

[19] M. E. Gehm, "Properties of $^6li$," 2003.

[20] W. I. McAlexander, E. R. I. Abraham, and R. G. Hulet, "Radiative lifetime of the $2P$ state of lithium," *Phys. Rev. A*, vol. 54, p. R5, July 1996.

[21] R. Grimm, M. Weidemller, and Y. B. Ovchinnikov, "Optical dipole traps for neutral atoms," *Molecular and Optical Physics*, vol. 45, pp. 95–170, 2000.

[22] D. Griffiths, *Introduction to Quantum Mechanics (2nd Edition)*. Pearson Prentice Hall, 2004.

[23] A. Derevianko, J. Babb, and A. Dalgarno, "High-precision calculations of van der waals coefficients for heteronuclear alkali-metal dimers," *Phys. Rev. A*, vol. 63, p. 052704, 2001.

[24] C. Chin, R. Grimm, P. Julienne, and E. Tiesinga, "Feshbach resonances in ultra-cold gases," *Rev. Mod. Phys.*, vol. 82, p. 12251286, 2010.

[25] G. Zrn, T. Lompe, A. N. Wenz, S. Jochim, P. S. Julienne, and J. M. Hutson, "Precise characterization of li6 feshbach resonances using trap- sideband-resolved rf spectroscopy of weakly bound molecules," *Phys. Rev. Lett.*, vol. 110, p. 135301, 2013.

[26] T. Walker, D. Sesko, and C. Wieman, "Collective behavior of optically trapped neutral atoms," *Phys. Rev. Lett.*, vol. 64, p. 408, 1990.

[27] J. Dalibard and C. Cohen-Tannoudji, "Laser cooling and trapping of neutral atoms," *Rev. Mod. Phys.*, vol. 70(3), pp. 721–741, 198.

[28] W. D. Phillips and H. Metcalf, "Laser deceleration of an atomic beam," *Phys. Rev. Lett.*, vol. 48, pp. 596–599, 1982.

[29] A. Burchianti, G. Valtolina, J. A. Seman, E. Pace, M. D. Pas, M. Inguscio, M. Zaccanti, and G. Roati, "Efficient all-optical production of large $^6li$ quantum gases using $d_1$ gray-molasses cooling," *Phys. Rev. A*, vol. 90, p. 043408, 2014.

[30] F. Sievers, N. Kretzschmar, D. R. Fernandes, D. Suchet, M. Rabinovic, S. Wu, C. V. Parker, L. Khaykovich, C. Salomon, and F. Chevy, "Simultaneous sub-doppler laser cooling of fermionic $^6$li and $^4$0k on the $d_1$ line: Theory and experiment," *Phys. Rev. A*, vol. 91, p. 023426, 2015.

[31] G. Salomon, L. Fouch, P. Wang, P. B. A. Aspect1, and T. Bourdel, "Gray-molasses cooling of $^3$9k to a high phase-space density," *EPL (Europhysics Letters)*, vol. 104(6), p. 023426, 2014.

[32] J. Dalibard and C. Cohen-Tannoudji, "Laser cooling below the doppler limit by polarization gradients: simple theoretical models," *Optical Society of America B*, vol. 6.

[33] H. J. Metcalf and P. van der Straten, *Laser Cooling and Trapping*. Springer.

[34] R. Grimm, M. W. uller, and Y. B. Ovchinnikov, "Optical dipole traps for neutral atoms," *Adv. At. Mol. Opt. Phys.*, vol. 42, pp. 95–170, 2000.

[35] W. Ketterle and N. J. V. Druten, "Evaporative cooling of trapped atoms," *Advances In Atomic, Molecular, and Optical Physics*, vol. 37, p. 181 236, 1986.

[36] W. Petrich, M. H. Anderson, J. R. Ensher, and E. A. Cornell, "Stable, tightly confining magnetic trap for evaporative cooling of neutral atoms," *Phys. Rev. Lett.*, vol. 74, p. 33523355, 1995.

[37] S. Chaudhuri, S. Roy, and C. S. Unnikrishnan, "Evaporative cooling of atoms to quantum degeneracy in an optical dipole trap," *J. Phys. Conf. Ser.*, vol. 80, p. 012036, 2007.

[38] K. OHara, M. Gehm, S. Granade, and J. Thomas, "Scaling laws for evaporative cooling in time-dependent optical traps," *Phys. Rev. A.*, vol. 64, p. 051403, 2001.

[39] W. Ketterle, D. Durfee, and D. Stamper-Kurn, "Making, probing and understanding bose-einstein condensates," *arXiv:cond-mat/9904034*.

[40] C. Pethick and H. Smith, "Bose-einstein condensation in dilute gases (second edition)," *Cambridge University Press*, 2008.

[41] S. Warriar, *Towards an Ultracold Bose-Fermi Mixture of Cesium and Lithium Atoms*. PhD thesis, University of Nottingham, 2014.

[42] D. S. Petrov, C. Salomon, and G. V. Shlyapnikov, "Weakly bound dimers of fermionic atoms," *Phys. Rev. Lett.*, vol. 93, p. 090404, 2004.

[43] K. E. Strecker, *Tunable Interaction in Quantum Degenerate Lithium*. PhD thesis, Department of Physics, Rice University, 2004.

[44] C. Salomon, J. Dalibard, W. D. Phillips, A. Clairon, and S. Guellati, "Laser cooling of cesium atoms below 3 $\mu k$," *Europhys. Lett.*, vol. 12 (8(, pp. 683–688, 1990.

[45] K. Xhani, "Production and observation of degenerate quantum gases of $^6li$ fermionic atoms," Master's thesis, Universit degli studi di Firenze, 2014.

[46] F. Dalfovo, S. Giorgini, L. P. Pitaevskii, and S. Stringari, "Theory of bose-einstein condensation in trapped gases," *Reviews of Modern Physics*, vol. 71, 1999.

[47] L. Pitaevskii and S. Stringari, *Bose-Einstein Condensation. International Series of Monographs on Physics*. Oxford: Clarendon Press, 2003.

[48] N. Welch, *Non-Equilibrium Dynamics of Bose-Einstein Condensates*. PhD thesis, University of Nottingham, 2015.

[49] G. Valtolina, A. Burchianti, A. Amico, E. Neri, K. Xhani, J. A. Seman, A. Trombettoni, A. Smerzi, M. Zaccanti, M. Inguscio, and G. Roati, "Josephson effect in fermionic superfluids across the bec-bcs crossover," *Science*, vol. 250, pp. 1505 – 1508, 2015.

[50] M. Gajdacz, P. L. Pedersen, T. Mrch, A. J. Hilliard, J. Arlt, and J. Sherson, "Non-destructive faraday imaging of dynamically controlled ultracold atoms," *Review of Scientific Instruments*, vol. 84, p. 083105, 2013.

[51] A. Spuntarelli, P. Pieri, and G. C. Strinati, "Josephson effect throughout the bcs-bec crossover," *Phys. Rev. Lett.*, vol. 99, p. 040401, 2007.

[52] L. Salasnich, N. Manini, and F. Toigo, "Macroscopic periodic tunneling of fermi atoms in the bcs-bec crossover," *Phys. Rev. A*, vol. 77, p. 043609, 2008.

[53] J. Mumford and D. H. J. ODell, "Critical exponents for an impurity in a bosonic josephson junction: Position measurement as a phase transition," *Phys. Rev. A*, vol. 90, p. 063617, 2014.

[54] J. Mumford, J. Larson, and D. H. J. ODell, "Impurity in a bosonic josephson junction: Swallowtail loops, chaos, self-trapping, and dicke model," *Phys. Rev. A*, vol. 89, p. 023620, 2014.